Second-Order Coherence of Microwave Photons Emitted by a Quantum Point Contact

master's thesis

presented by

Daniel Otten

under the supervision of

Prof. Dr. Fabian Hassler

JARA-Institute for Quantum Information, RWTH Aachen University,
D-52056 Aachen, Germany

submitted to the

Faculty of Mathematics, Computer Science and Natural Sciences

November 10, 2015

Ich versichere, dass ich die Arbeit selbstständig verfasst und keine anderen als die angegebenen Quellen und Hilfsmittel benutzt sowie Zitate kenntlich gemacht habe.

Aachen, den 13. Juli 2023

Daniel Otten

Abstract

The particle nature of photons or electrons allows to do various types of counting experiments. The full counting statistics, describing how the particles are distributed, is completely determined by the cumulants of the distribution. Here, we present a diagrammatic approach to calculate current cumulants for the electron transport through a quantum point contact (biased at a voltage V_0). We provide compact expressions for cumulants up to and including the third order. Furthermore, fluctuations in the electronic current lead to emitted radiation in the microwave regime. In this context the current cumulants are linked to the photon counting statistics of the microwave field. For this setup, we calculate the Fano factor F and the second order coherence function $g^{(2)}(\tau)$. It has been shown that radiation produced by such kind of sources, at frequency ω_0 close to $eV_0/\hbar$, obeys sub-Poissonian statistics ($F < 1$), which cannot be understood in terms of classical radiation sources. We determine the critical temperature below which sub-Poissonian radiation may be observed. Being a time integrated quantity, the Fano factor carries less information than the time resolved second-order coherence function. We find that the latter shows a minimum for times $\tau \simeq \omega_0^{-1}$. In the vicinity of this time, $g^{(2)}(\tau)$ remains below 1 even at temperatures for which the Fano factor already approaches a classical value ($F > 1$).

Contents

Chapter 1

Introduction

1.1 Coherence of Electromagnetic Radiation

Interference measurements are an established tool in physics to gain information about sources of radiation of almost any type. The ordinary interference measurements concentrate on comparing the amplitudes of signals at a given point (as for example in Young's double slit experiment) [1]. Such amplitude-amplitude correlations quantify the first-order coherence of the signal. However, one can also compare the intensities of different signals, which gives rise to second-order coherence properties. This is referred to as Hanbury Brown and Twiss interferometry. In 1956 Hanbury Brown and Twiss introduced this new type of interferometry [2]. They found a correlation between the intensity of the signals coming from two uncorrelated sources measured with two spatially separated detectors. The correlation then depended on the distance between the two detectors. While this effect seemed acceptable in terms of classical physics, where light is described by waves, it gave people headaches when they thought about its quantum nature. The electromagnetic field is quantized with its quanta being photons, the 'particles of light'. A photon detector can be able to measure incoming photons one by one. It seemed awkward to have uncorrelated radiation sources sending non-interacting photons away, but when they arrive at the detectors the measurement is suddenly correlated. Therefore, some physicists could not accept the effect and published papers that doubt its existence [3]. However, the Hanbury Brown and Twiss effect (HBT effect) turned out to be real [4]. The confusion it caused only arises if one pictures photons as classical particles separated from each other, which they are not. Photons are bosons, which follow the Bose-Einstein statistics, and tend to arrive in bunches [4]. This bunching is a result from their statistics alone and does not need interactions. The quantum mechanical result agrees with the calculations obtained from the classical wave picture, just because the classical wave equations already capture the bosonic nature. However, as particles, bosons cannot be understood classically. Bosons deviate from classical particles with their positive correlation and in a similar way fermions like electrons deviate in the other direction and tend to antibunch. The controversy about the HBT effect led physicists to think about quantum electrodynamics and its usage in a

new way, which established the beginnings of the filed of quantum optics [1, 4]. Even today, there remain some unsolved challenges in this field. One of them is the measurement of antibunched photons. Classically typical electromagnetic radiation like thermal, chaotic or laser light always follows the HBT effect; thus, photons always arrive in bunches. However, in certain setups, quantum mechanics forces photons to anitbunch so that they, like fermions, tend to stay away from each other. This effect has only been measured for single atom like sources [5], but has not yet been observed for sources producing photons by something similar to the light bulb principle, where the resistance of a DC-voltage biased wire leads to photon production. Thus, it is of fundamental interest to find such sources producing non-classical radiation. The motivation for this work is to find a good theoretical model of such a non-classical radiation source and to provide theoretical information supporting the realization of photon antibunching experiments.

1.2 Quantum Point Contacts as Source of Radiation

Mesoscopic physics describes the physics in an intermediate regime between dealing with sizes of single particles and on the other side with macroscopic objects. Therefore, it is a good regime to find physical objects which can be implemented with acceptable and scaleable effort, but still obey quantum properties. A quantum point contact (QPC) is such an object. It is a small constriction in the transverse direction of a conductor of mesoscopic size, often realized in two dimensional electron gases. The spatial constraint leads to a quantization of the electronic states propagating through the QPC [6]. Today, QPCs are used in many experiments, for example as read out detectors in some types of quantum bits [7]. The central idea for the production of photons in this thesis is to use a QPC as a source of radiation. A voltage biased QPC induces current fluctuations, while these current fluctuations then produce photons. The transport properties of such a QPC can be described with the Landauer-Büttiker formalism of mesoscopic quantum transport [8]. With this, it is simple to describe currents through the QPC. Currents are naturally one of the most important observables in solid state physics. Their fluctuations are expressed by higher-order current cumulants, which are not only interesting for the usage of QPCs as source of radiation, but they determine the counting statistics of the electronic current. Therefore, it is of even broader interest to determine these cumulants independently from the usage of the QPC as a source of radiation.

1.3 Overview

In the following, we give a short outline of the thesis. In Chapter 2, we continue to discuss the coherence of electromagnetic radiation and give a little more detailed introduction to the HBT effect. We then introduce the Landauer Büttiker formalism, which we are using to describe the transport properties through the quantum point contact in Chapter 3. A major part of this work is the calculation of various current cumulants, with the purpose of determin-

ing the second-order coherence function. Therefore, in Chapter 4, we present a novel diagrammatic approach for the calculation of these cumulants. Furthermore, we present results for all current cumulants up to and including the third-order in a compact form. A 4th-order cumulant is presented approximately. Readers only interested in current cumulants can read this chapter almost independently from the aspect of photon antibunching. In Chapter 5 we present a model for a setup in which we find non-classical radiation. To validate the latter, we calculate the Fano factor and the second-order coherence function $g^{(2)}(\tau)$ for the expected photon rate measured by a photon detector. From this we determine two critical temperatures (one from the Fano factor and one from $g^{(2)}(\tau)$), below which non-classical radiation can be observed.

In Appendix A, we derive the so called polar decomposition and discuss the causality of the scattering matrix, which we use within the diagrammatic approach. In Appendix B, the reader finds a derivation for the diagrammatic rules we present already in Chapter 4. Finally in Appendix C, we list all current cumulants up and including the third-order.

Chapter 2

Second-Order Coherence

In this chapter, we want to give a detailed overview of the statistics of electromagnetic radiation we talked about in the introduction (which we sometimes refer to as statistics of light, independently from the wave length of the radiation). First we explain the HBT effect in little more detail, using a classical example. Then, we define some useful quantities like the second-order coherence function $g^{(2)}(\tau)$ and the Fano factor in a quantum mechanical sense. Finally, we introduce the idea of photon antibunching, which is the opposite behavior of the HBT effect.

2.1 Hanbury Brown and Twiss Effect

In this section, we explain the HBT effect with a classical example following [1]. The effect can be understood completely by the simple classical wave description of light. We imagine two uncorrelated sources of radiation a and b and two detectors A and B, as shown in Fig. 2.1. The two sources are assumed to be separated in space by a distance R while the two detectors are separated by a distance d. The distance between the source and the detectors L should be much larger than R and d. We assume the source a to produce a spherical signal

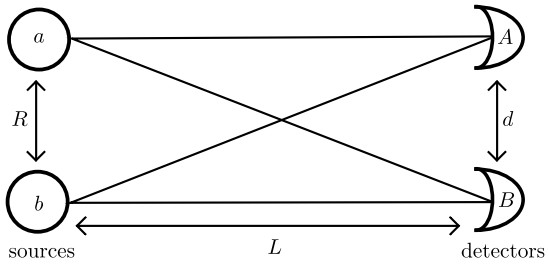

Figure 2.1: Sketch of the setup for a HBT interferometry measurement. Two uncorrelated sources a and b sending radiation (solid lines) to two detectors A and B. The detectors measure the intensity (or particle count) of the radiation. Later the results can be put together to calculate a possible correlation.

with amplitude $\alpha e^{ik(|\boldsymbol{r}|+\phi_a)}/L$ while source b produces the signal $\beta e^{ik(|\boldsymbol{r}|+\phi_b)}/L$. Here, $\boldsymbol{r}$ is the vector pointing from the detector to the source. The phases ϕ_a and ϕ_b are assumed to be random. We can write the full amplitude at detector A as a sum of the two partial waves

$$A_A = \frac{1}{L}\alpha e^{ik(r_{aA}+\phi_a)} + \beta e^{ik(r_{bA}+\phi_b)}, \tag{2.1}$$

with r_{aA} and r_{bA} the distance between the sources and detector A. The absolute square of A_A is proportional to the intensity measured at this detector and given by

$$I_A = \frac{1}{L^2}(|\alpha|^2 + |\beta|^2 + \alpha^*\beta e^{i[k(r_{aA}-r_{bA})+\phi_b-\phi_a]} + \alpha\beta^* e^{-i[k(r_{aA}-r_{bA})+\phi_b-\phi_a]}). \tag{2.2}$$

The result for I_B can be obtained by replacing A by B. When averaging over the random phases, the crossterms vanish and we find

$$I_A = A_A^2 = \frac{1}{L^2}(|\alpha|^2 + |\beta|^2) \tag{2.3}$$

so that all information about the phase is lost. However, when we multiply the intensities before averaging, we find an additional term proportional to $|\alpha|\,|\beta|$ which does not average out because its random phase dependence cancels out. We obtain the result

$$\langle I_A I_B\rangle = \frac{1}{L^2}(|\alpha|^4 + |\beta|^4 + 2\,|\alpha|^2\,|\beta|^2\,\{1+\cos[k(r_{aA}-r_{aB}-r_{bA}+r_{bB})]\}. \tag{2.4}$$

The last term in this expression now oscillates depending on the distances of the sources and the detectors. Normalizing the result with the simple product $\langle I_A\rangle\langle I_B\rangle$ we find

$$\begin{aligned}\frac{\langle I_A I_B\rangle}{\langle I_A\rangle\langle I_B\rangle} &= g^{(2)}(0)\\ &= 1 + \frac{2\,|\alpha|^2\,|\beta|^2}{(|\alpha|^2+|\beta|^2)^2}\cos[k(r_{aA}-r_{aB}-r_{bA}+r_{bB})]),\end{aligned} \tag{2.5}$$

where we defined $g^{(2)}(0) = g^{(2)}(\tau = 0)$ to be the classical second-order coherence function with zero time delay. Multiplying the intensities at different times, then introduces the delay time τ. With this kind of measurement, one can get information about the distance of the sources for example. The same experiment can also be done with a single detector. Then, the distance between detector A and B is zero and thus the argument of the cosine is also zero, rendering $\cos[k(r_{aA}-r_{aB}-r_{bA}+r_{bB})] = 1$. As the prefactor of the cosine is always positive, we see that in this case

$$g^{(2)}(0) \geq 1, \tag{2.6}$$

which can be shown to hold in all cases [9]. Furthermore, for all kinds of chaotic light for which the resulting field is a superposition of coherent sources with a random phase distribution as in the above example, it is found that

$$g^{(2)}(\tau) \geq 1 \tag{2.7}$$

holds for all τ.

It was easy to show that in our example the intensities tend to be positively correlated, which translates into the the Hanbury Brown and Twiss effect/bunching of photons. This effect also occurs if one uses a quantum mechanical description, even if it feels more counter intuitive then. In the next section, we define the quantum mechanical version of $g^{(2)}(\tau)$ and the Fano factor to classify photon number distributions.

2.2 Defining the Second-Order Coherence Function

Having explained the HBT effect in classical language, we now define the Fano fator and the second-order coherence functions, which is the normalized photon photon correlation function in a quantum mechanical sense. Then, we are interested in what their outcomes say about the statistics of different light sources. All quantities we define in this section are meant to be measured by a single detector with only a small extent in space. This corresponds to the case in Section 2.1, where we assumed the detectors A and B to be at the same spot. When we talk about statistics of electromagnetic radiation, we mean counting statistics and therefore the photon number distribution of an electromagnetic field. A quantum mechanical light field does not need to have a defined number of photons, it can also be in a superposition of having different photon numbers. A photon detector can then in principle detect single photons arriving. The rate of photon arrival corresponds to the photon number in the field which is in contact with the detector. Therefore, it is useful to have quantities which classify different photon distributions in a simple way. First, we want to define the Fano factor, which is a time integrated quantity and given by

$$F = \frac{\langle (\delta N)^2 \rangle}{\langle N \rangle} = \frac{\langle N^2 \rangle - \langle N \rangle^2}{\langle N \rangle}, \tag{2.8}$$

where $\langle N \rangle$ is the total photon count detected in the measurement time and $\langle (\delta N)^2 \rangle$ its variance (with $\delta N = N - \langle N \rangle$). It can be understood as a signal to noise ratio. We call a radiation field Poissonian if it has a Poissonian photon number distribution with the variance equivalent to the mean value and thus $F = 1$. A field with $F < 1$ is then called to be sub-Poissonian and a field with $F > 1$ is called to be super-Poissonian. To give an example, the photon distribution in laser light obeys a Poissonian distribution. In contrast, when we look at a Fock state with a defined number of photons, we obviously have a vanishing variance and therefore also the Fano factor vanishes so that $F = 0$. As the variance and also the mean photon number are always positive, this is the lower limit for the Fano factor.

The probably most common source of radiation is thermal radiation. For this we can calculate the mean photon number in a blackbody cavity by

$$\langle n_{\mathrm{cav}} \rangle = \frac{1}{Z} \sum_n e^{-\hbar\omega n_{\mathrm{cav}}/k_B\vartheta} n = \frac{1}{e^{\hbar\omega/k_B\vartheta} - 1}, \tag{2.9}$$

with $Z = \sum_n e^{-\hbar\omega n_{\mathrm{cav}}/k_B\vartheta}$ and ϑ the temperature. This is just the Bose-Einstein distribution. With the same kind of calculation we find

$$\langle (\delta n_{\mathrm{cav}})^2 \rangle = \frac{e^{\hbar\omega/k_B\vartheta}}{(e^{\hbar\omega/k_B\vartheta} - 1)^2}. \tag{2.10}$$

To connect the number of photons in the cavity n_{cav} to the number of photons registered by the detector outside the cavity N in the measurement time T_M, we assume the event of photons leaving the cavity to occur at a small rate γ. This way, single emission events can be assumed to be uncorrelated. Then we can express $\langle N \rangle = \langle n_{\mathrm{cav}} \rangle \gamma T_M$ and $\langle (\delta N)^2 \rangle = \langle (\delta n_{\mathrm{cav}})^2 \rangle \gamma T_M$. Using this together with (2.9) and (2.10) we find $F = \langle N \rangle + 1$. We have $F > 1$, classifying thermal light as super-Poissonian, which is shown below to correspond to photon bunching. In contrast, it is an aim of this work to find a similar source that gives rise to photon antibunching caused by quantum effects. Additionally, we also see from this example that the Fano factor can scale with the signal intensity because the latter is proportional to the number of photons.

Another important quantity is the quantum mechanical version of $g^{(2)}(\tau)$ for which we already discussed the classical pendant. In quantum mechanics it is a measure for the conditional probability of finding a photon at time $t = \tau$ if one already registered a click in the detector at time $t = 0$. It is given by the normalized photon number correlation function and defined as

$$g^{(2)}(\tau) = \frac{\langle :n(\tau)n(0): \rangle}{\langle n \rangle^2}, \tag{2.11}$$

where $n(\tau)$ is the operator for the instantaneous photon number rate registered by a photon detector at the delay time τ. It is connected to the measured number of photons in the measurement time T_M by

$$N = \int_0^{T_M} d\tau \; n(\tau). \tag{2.12}$$

The colons in (2.11), not present in the classical expression, denote a normal ordering so that all creation operators in the expression [the operator $n(\tau)$ can be decomposed into bosonic creation and annihilation operators like $n(\tau) = a^\dagger(\tau)a(\tau)$, which do not correspond to the later introduced fermionic operators] are moved to the left of annihilation operators. In principle we needed to do a Keldysh time ordering for such measurable physical quantities like $g^{(2)}(\tau)$. However, in quantum optics the photon numbers are measured by a photon detector which clicks when it absorbs the energy quantum of a photon. This process corresponds to the annihilation of the photon in the electromagnetic field. When taking only the annihilation operators of the filed into account,

it turns out that the Keldysh time ordering can be reduced to the normal ordering indicated by the colons. As we always assume a stationary state in this work, $g^{(2)}(\tau)$ only depends on the delay time τ but not on the explicit measurement time t. In most cases, there is a correlation delay time τ_c after which all correlations are almost lost with $\left[g^{(2)}(\tau \gg \tau_c) - 1\right] \propto \exp(-\tau/\tau_c)$. Furthermore, one can show that for radiation with fluctuations independent of the optical phase $1 \leq g^{(2)}(\tau) < \infty$ [10]. This is valid for various kinds of radiation, like chaotic radiation, thermal radiation or laser light. For the latter, the equality to one is fulfilled (with a Poissonian distribution) and the state is called to be second-order coherent. The inequality can also be explained classically by assuming the measured results to be the superposition of coherent fields with different intensities leading to Eq. (2.7). So whenever the second-order coherence takes a value below one, a classical description as described above cannot explain the result. Therefore, it is justified to speak of non-classical radiation in most such examples.

Now, it is easy to establish a connection between the two quantities we have defined. With the insight of [11], the Fano factor can be expressed by $g^{(2)}(\tau)$ as

$$F - 1 = \langle n \rangle \int d\tau \, [g^{(2)}(\tau) - 1]. \tag{2.13}$$

This can be seen when we rewrite the right-hand side as

$$F - 1 = \int d\tau \, \frac{\langle :n(\tau)n(0): \rangle - \langle n \rangle^2}{\langle n \rangle}. \tag{2.14}$$

The mean photon number rate $\langle n(t) \rangle = \langle n \rangle$ is constant over time (because we are looking at steady states) and can be taken inside the integral. For times $\tau \gg \tau_c$ the right-hand side is zero. Therefore, we can replace the integration over the full time $-\infty < \tau < \infty$ by the integration over the measurement time $-T_M < \tau < T_M$, as long as $T_M \gg \tau_c$. Additionally with the fact that for a stationary state the correlation function $\langle :n(\tau)n(0): \rangle$ only depends on the delay time τ we find for long measurement times T_M

$$\begin{aligned} \int d\tau \langle :n(\tau)n(0): \rangle &= \frac{1}{T_M} \iint_0^{T_M} dt_1 dt_2 \, \langle :n(t_1)n(t_2): \rangle \\ &= \frac{1}{T_M} \left[\iint_0^{T_M} dt_1 dt_2 \, \langle n(t_1)n(t_2) \rangle - \int_0^{T_M} dt \, \langle n \rangle \right], \end{aligned} \tag{2.15}$$

where we rearranged the normal ordered creation and annihilation operators in $\langle :n(\tau)n(0): \rangle$ in the last step. This way we find

$$\begin{aligned} F &= \frac{\langle N^2 \rangle}{\langle N \rangle} - \frac{\langle N \rangle^2}{\langle N \rangle} \\ &= \frac{\langle (\delta N)^2 \rangle}{\langle N \rangle}. \end{aligned} \tag{2.16}$$

Both, the Fano factor and $g^{(2)}(\tau)$, carry information about the statistical distribution of the radiation. However, $g^{(2)}(\tau)$ also encodes information for example

about the correlation time, which the Fano factor does not. We see that for Poissonian distributed radiation with $g^{(2)}(\tau) = 1$ the Fano factor come out as expected with $F = 1$. Furthermore, if $g^{(2)}(\tau) < 1$ for a finite time interval $[\tau_1, \tau_2]$, then also the Fano factor can take values below one. However, when $g^{(2)}(\tau) > 1$ for all times, we have a Fano factor that has to be larger than one. Therefore, the Fano factor is linked with the counting statistics and can already indicate if we deal with classical or non-classical radiation.

2.3 Photon Antibunching

The Hanbury Brown and Twiss effect accounts for the bunching of photons with $g^{(2)}(\tau) \geq 1$. However, as already announced in the introduction, in some setups there can also be negative photon-photon correlations even at zero delay time. A simple example for such a non-classical state is a single mode Fock state $|n\rangle$ with $\langle(\delta n)^2\rangle = 0$. For such a state the second-order coherence is given by [9] as

$$\begin{aligned} g^{(2)}(\tau) = g^{(2)}(0) &= 1 + \frac{(\delta n)^2 - \langle n\rangle}{\langle n\rangle^2} \\ &= 1 - \frac{1}{n} \end{aligned} \tag{2.17}$$

for $n \neq 0$ and $g^{(2)}(\tau) = 0$ for $n = 0$. One immediately sees that these values for the second-order coherence function violate the classical inequalities $g^{(2)}(0) \geq 1$ and thus give rise to a quantum mechanical effect. However, in this case $g^{(2)}(\tau)$ is a constant and therefore photons tend to be found in equidistant time steps. In reality, the photon detector destroys a photon in the state it measures and therefore a Fock state changes over time, so that it is difficult to speak about stationary states in this example. In this thesis, we are especially interested in finding a stationary state for which one can measure non-classical counting statistics. The concrete aim of this work is to provide a model for a setup in which antibunching photons are emitted and can be detected. The rough idea for the preparation of these states is to produce radiation with electronic current fluctuations. This current fluctuations are caused by a constant bias voltage over a quantum point contact similar to the concept of a light bulb. Engineering an environment which filters only for photons around the frequency given by the bias voltage suppresses the possibility of an electron emitting two photons at once. This is because the electrons should have an energy around the bias voltage and lose directly all of it, when they produce photons in the frequency regime of the bias voltage. The electrons however are Fermions and naturally antibunch; When a single electron approximately produces a single photon, they should also show antibunching behavior. A more detailed explanation is given in Chapter 5.

Chapter 3

Transport Through the QPC

In the introduction, we have already mentioned QPCs as possible sources for radiation producing antibunching photons. In this chapter, we want to introduce the formalism that we use to calculate the transport properties of QPCs. Therefore, we first introduce very shortly the Landauer Büttiker formalism. After this, we briefly explain Wick's theorem, which we use to calculate many-operator expectation values.

3.1 Landauer Büttiker Formalism

In this work, we deal with a non-equilibrium situation where a current flows through a quantum point contact between two large electron reservoirs each in their own local equilibrium. The Landauer Büttiker formalism treats this by reducing the problem to the calculation of separate equilibrium quantities of the first and the second reservoir. The presented formalism can also deal with multi terminal problems (more than two reservoirs) but in this work we only use the two terminal approach. Therefore, only the latter is presented here, for which we follow mainly [12] .

The main idea is based on a scattering approach introduced by Landauer. In Figure 3.1 we show the setup we have in mind when explaining the formalism in

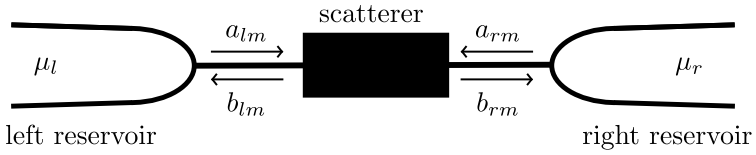

Figure 3.1: Sketch for a two terminal transport setup in the Landauer Büttiker approach. Two electron reservoirs, each in their own equilibrium with chemical potential μ_l and μ_r, are connected by a phase coherent conductor with a quantum mechanical scatterer in the middle. The arrows indicate the incoming modes, going from the reservoirs to the scatterer, and the outgoing modes, propagating the other way around.

this chapter. We have two large leads connected by a phase coherent conductor with a small mesoscopic sample in between (in this work a quantum point contact). The leads are labeled by 'l' for the left lead and by 'r' for the right lead. Each of them is large compared to the mesoscopic sample so that we can assume them to be in their own local equilibrium. Thus, they can be described by the temperature ϑ and a chemical potential μ_α with $\alpha \in \{l, r\}$. The particles in each lead are distributed according to the Fermi distribution

$$f_\alpha(\varepsilon) = \{e^{[(\hbar\varepsilon - \mu_\alpha)/k_B\vartheta]} + 1\}^{-1}, \tag{3.1}$$

where k_B is the Boltzmann constant. For convenience we also define the function

$$g_\alpha(\varepsilon) = 1 - f_\alpha(\varepsilon) = \{e^{[(-\hbar\varepsilon + \mu_\alpha)/k_B\vartheta]} + 1\}^{-1}. \tag{3.2}$$

In the following, we refer to both of them with f- and g-Fermi functions. Furthermore, we define a difference function of the Fermi distributions

$$\Delta(\varepsilon) = f_r(\varepsilon) - f_l(\varepsilon) = g_l(\varepsilon) - g_r(\varepsilon), \tag{3.3}$$

which turns out very useful to express results more compactly. Even though the leads are in their own local equilibrium, the whole system is in a non-equilibrium state because the phase coherent conductor slightly connects the two reservoirs. The latter act as sources and sinks for carriers. Carriers leaving the left reservoir are assumed to be distributed according to the Fermi function of the left reservoir. Then, they are scattered at the sample according to a scattering matrix that in principle has to be determined for each scatterer by a quantum mechanical calculation. When they enter the right reservoir, they are assumed to not significantly disturb the equilibrium there. Then, they relax to the equilibrium state of the right lead so that whenever they return to the scatterer, they are distributed according to the right Fermi function. The same is valid for for carriers starting in the right reservoir. The relaxation in the opposite lead is the mechanism in this formalism that introduces dissipation and irreversibility. This explicitly breaks time-reversal invariance.

Far away from the sample, it is possible to assume that the spatial wave function of the carriers can be separated into a longitudinal (from left to right) and a transverse part. The longitudinal part in the perfect conductor can be described by plane waves $e^{ik_l z}$ with the wave vector k_l and the longitudinal coordinate z. The transverse part is quantized due to the spatial constriction with its different levels labeled by the quantum number m so that the total energy is given by $\hbar\varepsilon = \hbar(\varepsilon_m + \varepsilon_{k_l})$. We also separate the longitudinal part of the states into incoming states and outgoing states from the viewpoint of the sample. They correspond to a longitudinal motion from the lead to the sample (incoming) and from the sample to the lead (outgoing). The easiest way to describe this fact is to use a second quantized formalism. We introduce the operators $a^\dagger_{\alpha,m}(\varepsilon)$ and $a_{\alpha,m}(\varepsilon)$, creating (annihilating) an incoming state with total energy ε on the side given by α, and the operators $b^\dagger_{\alpha,m}(\varepsilon)$ and $b_{\alpha,m}(\varepsilon)$,

creating (annihilating) an outgoing state at energy ε on the side given by α. They are both fermionic operators and obey the anticommutation relations

$$\begin{aligned}\{a_{l,m}(\varepsilon), a^\dagger_{l,m'}(\varepsilon')\} &= \delta_{m,m'}\delta(\varepsilon-\varepsilon')\\ \{a_{l,m}(\varepsilon), a_{l,m'}(\varepsilon')\} &= 0\\ \{a^\dagger_{l,m}(\varepsilon), a^\dagger_{l,m'}(\varepsilon')\} &= 0\end{aligned} \tag{3.4}$$

and similar for $b^\dagger_{l,m}(\varepsilon)$ and $b_{l,m}(\varepsilon)$. The same relations hold for the operators corresponding to the right reservoir. The outgoing and incoming states are connected by the scattering matrix $S(\varepsilon)$:

$$\begin{pmatrix} b_{l,1}(\varepsilon)\\ \vdots\\ b_{l,N_l}(\varepsilon)\\ b_{r,1}(\varepsilon)\\ \vdots\\ b_{r,N_r}(\varepsilon)\end{pmatrix} = S(\varepsilon)\begin{pmatrix} a_{l,1}(\varepsilon)\\ \vdots\\ a_{l,N_l}(\varepsilon)\\ a_{r,1}(\varepsilon)\\ \vdots\\ a_{r,N_r}(\varepsilon)\end{pmatrix}, \tag{3.5}$$

with

$$S(\varepsilon) = \begin{pmatrix} r & t'\\ t & r'\end{pmatrix}. \tag{3.6}$$

Here r is a square matrix of the size $(N_l \times N_l)$, while r' is of the size $(N_r \times N_r)$. These blocks describe the reflection at the sample, transforming incoming states into outgoing states that end up in their starting reservoir. The off diagonal blocks t with size $(N_r \times N_l)$ and t' with size $(N_l \times N_r)$ describe the transmission from one side to the other through the mesoscopic sample. All components of the matrix depend on the matrix energy argument ε. Note that $S(\varepsilon)$ is a unitary matrix. In this work, we are especially interested in the current through a mesoscopic sample. As given in [12], the current operator in the right lead can be defined as

$$I_r(t) = e\sum_m \int \frac{d\omega}{2\pi}\int d\varepsilon\; e^{-i\omega t}\big[a^\dagger_{r,m}(\varepsilon)a_{r,m}(\varepsilon+\omega) - b^\dagger_{r,m}(\varepsilon)b_{r,m}(\varepsilon+\omega)\big]. \tag{3.7}$$

There is no difference in carrying out the calculations with the current in the right or in the left lead because of the fact that current is conserved. All currents entering the sample have to add up to zero. Therefore, the right current has to be equivalent to the left current. We arbitrarily choose to concentrate on the current on the right side. To make use of the fact that the incoming states are in an equilibrium, we use the scattering matrix to express the outgoing modes with the incoming modes and arrive at the expression

$$\begin{aligned}I_r(t) =& e\sum_m \int \frac{d\omega}{2\pi}\int d\varepsilon\; e^{-i\omega t}\\ &\times\Big[a^\dagger_{r,m}(\varepsilon)a_{r,m}(\varepsilon+\omega) - \sum_{n,\alpha,\beta,j} a^\dagger_{\alpha,m}S^\dagger_{r\alpha;mj}(\varepsilon)S_{r\beta;jn}(\varepsilon+\omega)a_{\beta,n}(\varepsilon+\omega)\Big].\end{aligned} \tag{3.8}$$

Here $\alpha, \beta \in \{l, r\}(\varepsilon)$ label the left or right reservoir. The matrix $S_{l\beta;jn}$ translates $b_{l,j}(\varepsilon)$ to $a_{\beta,n}(\varepsilon)$. It is convenient to divide the current into incoming and outgoing currents. The incoming current is created by the incoming states while the outgoing current is consequently created by the outgoing states. Thus, we can write

$$\begin{aligned} I_{\text{in}}(t) =& e \sum_m \int \frac{d\omega}{2\pi} \int d\varepsilon e^{-i\omega t} a^\dagger_{r,m}(\varepsilon) a_{r,m}(\varepsilon + \omega), \\ I_{\text{out}}(t) =& e \sum_{\substack{m,n,\\ j,\alpha,\beta}} \int \frac{d\omega}{2\pi} \int d\varepsilon \; e^{-i\omega t} a^\dagger_{\alpha,m}(\varepsilon) S^\dagger_{r\alpha;mj}(\varepsilon) S_{r\beta;jn}(\varepsilon + \omega) a_{\beta,n}(\varepsilon + \omega), \end{aligned} \tag{3.9}$$

so that $I = I_{\text{in}} - I_{\text{out}}$. From now on we can use the equilibrium formalism to calculate arbitrary expectation values with current operators. When we proceed with this, we have to evaluate expectation values of products of creation and annihilation operators for a system in thermal equilibrium. For an ideal Fermi gas (which is a good approximation for a perfect conductor) such are given by the simple expressions

$$\begin{aligned} \langle a^\dagger_{\alpha,m}(\varepsilon) a_{\beta,n}(\varepsilon') \rangle &= \delta_{\alpha\beta}\delta_{mn}\delta(\varepsilon - \varepsilon') f_\alpha(\varepsilon), \\ \langle a_{\alpha,m}(\varepsilon) a^\dagger_{\beta,n}(\varepsilon') \rangle &= \delta_{\alpha\beta}\delta_{mn}\delta(\varepsilon - \varepsilon') g_\alpha(\varepsilon). \end{aligned} \tag{3.10}$$

In principle, the scattering matrix is always energy dependent. However, often it is sufficient to treat it energy independent. This is the case if the matrix elements vary only slowly on the energy scales given by eV_0 or $k_B\vartheta$. When doing so, one has to take care because the scattering matrix does not only connect outgoing with incoming modes, it also ensures causality. By dropping the energy dependence of the scattering matrix we also drop its causality. However, this can be treated by using the correct time ordering. In the next chapter and in Appendix A we give a more detailed explanation. An energy independent scattering matrix simplifies the calculations a lot. We can use the so-called polar decomposition that states that we can use a basis of the scattering matrix in which it has a block diagonal structure. For each transverse mode m there is a separate block. Thus, the scattering matrix is the direct sum

$$S = \bigoplus_m S_m = \bigoplus_m \begin{pmatrix} r_m & t'_m \\ t_m & r'_m \end{pmatrix} \tag{3.11}$$

so that there is no scattering between transverse modes but only transmission and reflection between the longitudinal modes. Hence, the matrix elements of each submatrix S_m are simply complex numbers. The unitarity of S_m allows to choose the basis so that S is given by

$$S_m = \begin{pmatrix} \sqrt{R_m} & \sqrt{T_m} \\ -\sqrt{T_m} & \sqrt{R_m} \end{pmatrix}, \tag{3.12}$$

with $R_m = |r_m|^2$ and $T_m = |t_m|^2$. The parameters R_m and T_m correspond to the reflection and transmission probability of the mode m through the conductor.

They obey the relation $R+T=1$. A derivation of the polar decomposition and (3.12) can also be found in Appendix A. With this, we can rewrite the outgoing current as

$$I_{\text{out}}(\omega) = e\sum_m \int d\varepsilon \left\{ R_m a^\dagger_{r,m}(\varepsilon) a_{r,m}(\varepsilon+\omega) + T_m a^\dagger_{l,m}(\varepsilon) a_{l,m}(\varepsilon+\omega) \right. \\ \left. - R_m^{\frac{1}{2}} T_m^{\frac{1}{2}} [a^\dagger_{l,m}(\varepsilon) a_{r,m}(\varepsilon+\omega) + a^\dagger_{r,m}(\varepsilon) a_{l,m}(\varepsilon+\omega)] \right\}. \tag{3.13}$$

Here, we show the current in frequency space, which corresponds to the current in Eq. (3.9) when performing a Fourier transformation in ωt. The incoming current is unaffected by the approximation of the scattering matrix and reads in frequency space

$$I_{\text{in}}(\omega) = e\sum_m \int d\varepsilon \; a^\dagger_{r,m}(\varepsilon) a_{r,m}(\varepsilon+\omega). \tag{3.14}$$

From the fact that the current operators are Hermitian ($I(t) = I^\dagger(t)$), it follows

$$I(\omega)^\dagger = I(-\omega). \tag{3.15}$$

For the rest of this thesis, we choose $\mu_r = 0$ and $\mu_l = eV_0$, where V_0 is the voltage bias over the quantum point contact.

3.2 The Wick Theorem

For the evaluation of expectation values of more than one current operator in the Landauer Büttiker approach, which means more than two fermionic operators, we can use Wick's theorem. It provides a scheme on how to express expectation values of many fermionic creation and annihilation operators by a sum of all possible products of two operator correlation functions. It is valid if one calculates the equilibrium mean value in respect to Gaussian distributed systems (non-interacting systems) like the ideal Fermi gas in the Landauer Büttiker approach. In this section, we shortly explain how we use Wick's theorem in this work; a derivation can be found for example in [13].

If we have to calculate for example the value of $\langle O_1 O_2 \rangle$, where all O-operators consist of fermionic creation and annihilation operators like $O_i = c_i c_i^\dagger$, we proceed as

$$\langle c_1 c_1^\dagger c_2 c_2^\dagger \rangle = \langle c_1 c_1^\dagger \rangle \langle c_2 c_2^\dagger \rangle - \langle c_1 c_2 \rangle \langle c_1^\dagger c_2^\dagger \rangle + \langle c_1 c_2^\dagger \rangle \langle c_1^\dagger c_2 \rangle. \tag{3.16}$$

The example shows that we have to sum over all combinations of products of two-operator expectation values. Then, the sign of each term has to be determined separately. Before taking the average for each single combination, we have to rearrange the operators so that the ones which are averaged together are located next to each other. For each operator swap the term is multiplied by a factor of (-1). While doing the rearrangement, one may not commute two operators which are evaluated together in one expectation value. In our case,

the example above can be further simplified. The second term equals to zero, so we are left with

$$\langle c_1 c_1^\dagger c_2 c_2^\dagger \rangle = \langle c_1 c_1^\dagger \rangle \langle c_2 c_2^\dagger \rangle + \langle c_1 c_2^\dagger \rangle \langle c_1^\dagger c_2 \rangle. \tag{3.17}$$

This is based on the fact that the particle number is fixed in an ideal Fermi gas so that only expectation values with the same number of creation and annihilation operators can be evaluated finite. With this approach, we can easily express all expectation values in terms of f- and g- Fermi functions.

We now define a double bracket expectation value

$$\langle\langle O_1 O_2 \rangle\rangle_O := \langle O_1 O_2 \rangle - \langle O_1 \rangle \langle O_2 \rangle. \tag{3.18}$$

Calculating such a double bracket with Wick's theorem means to leave out all parings, where one would pair operators inside O_1 or O_2 alone. The terms calculated by this double bracket are then O-irreducible, thus one cannot split these terms in expectation values of only O_1- or only $\mathcal{O}_2$-operators. This notation can be scaled up for any number of operators:

$$\begin{aligned}\langle\langle O_1 O_2 O_3 \rangle\rangle_O :=& \langle O_1 O_2 O_3 \rangle - \langle\langle O_1 O_2 \rangle\rangle \langle O_3 \rangle \\ &- \langle\langle O_1 O_3 \rangle\rangle \langle O_2 \rangle - \langle\langle O_2 O_3 \rangle\rangle \langle O_1 \rangle - \langle O_1 \rangle \langle O_2 \rangle \langle O_3 \rangle.\end{aligned} \tag{3.19}$$

Whenever we use double brackets without an indicating operator, we consider current irreducible expressions. Double brackets can often be calculated easier than the full expectation values. We can then express the desired results with these.

Chapter 4

Calculation of Current Cumulants

Different cumulants of current operators will be central objects for the calculations in this work. Therefore, we treat them more generally in this separated chapter and use the results throughout the thesis. However, the whole chapter can also be read independently from the aspect of photon antibunching. The expressions we are interested in are of the form

$$C^{(n)}_{\eta_1\dots\eta_n}(t_1,t_2\dots t_n) = \langle\langle \mathcal{T}_C I^{\eta_1}(t_1) I^{\eta_2}(t_2)\dots I^{\eta_n}(t_n)\rangle\rangle, \tag{4.1}$$

or the equivalent expression in frequency space

$$C^{(n)}_{\eta_1\dots\eta_n}(\omega_1,\omega_2\dots\omega_n) = \langle\langle \mathcal{T}_C I^{\eta_1}(\omega_1) I^{\eta_2}(\omega_2)\dots I^{\eta_n}(\omega_n)\rangle\rangle. \tag{4.2}$$

Here, we have introduced the current I^η with $\eta \in \{+,-\}$. This notation is important for the time-ordering process when acting with the operator $\mathcal{T}_C$, which realizes a Keldysh time ordering. This time ordering arises, when modeling a detector for a measurement of the given cumulants [14]. Strictly speaking, detector theory tells us that the correct time ordering process is to act with $\mathcal{T}_C$ on the charge operators, which are the time integrated current operators. As long as the strict causality of the scattering matrix holds, time ordering on currents and charges can be shown to be identical [15]. Strict causality means that an incoming current can cause an outgoing current only to a later time. The word 'strict' also excludes equal time effects. As explained already in Chapter 3, it is often convenient and sufficient to treat the scattering matrix energy independent. However, by doing so, one drops its property of strict causality and the time ordering on current and on charge operators can differ. Yet, it was recently shown in [15, 16] that the in-out current ordering formalism, which we use below, is always equivalent to the physical ordering of charge operators. First we discuss how this time-ordering works explicitly. Then, we present a diagrammatic approach for the calculations of higher-order cumulants and use the formalism on explicit examples.

4.1 Keldysh Time Ordering

Acting on the current operators, $\mathcal{T}_C$ orders all currents $I^+(t)$ to the right and $I^-(t)$ to the left. Additionally, it does a time-ordering among the former and an anti-time-ordering among the latter. Now, we are confronted with the question, on how $\mathcal{T}_C$ acting in the frequency space is defined. This problem can be solved by exploiting the causality of the current operators and using the commutation relations of the incoming and outgoing currents. An incoming current at t_1 should not cause an outgoing current at an earlier or the same instant of time $t_2 \leq t_1$. From this follows that the incoming and outgoing parts of the currents $I(t_1)$ and $I(t_2)$ obey the commutation relations

$$\begin{aligned} [I_{\text{in}}(t_1), I_{\text{out}}(t_2)] &= 0 \quad \text{if } t_2 < t_1, \\ [I_{\text{in}}(t_1), I_{\text{in}}(t_2)] &= 0, \\ [I_{\text{out}}(t_1), I_{\text{out}}(t_2)] &= 0. \end{aligned} \tag{4.3}$$

The relations are a result of the property $S(t) = 0$ for $t \leq 0$, which guarantees the strict causality of the currents mentioned above. For more details on the derivation of these commutators see [17] and Appendix A. The presented commutation relations can be used to simplify the pure time-ordering process on the $\pm$-branch of the Keldysh contour. We denote the pure time-ordering operator as $\mathcal{T}$. Its action on an incoming and an outgoing current is generally given by

$$\mathcal{T} I_{\text{in}}(t_1) I_{\text{out}}(t_2) = I_{\text{in}}(t_1) I_{\text{out}}(t_2)\theta(t_1 - t_2) + I_{\text{out}}(t_2) I_{\text{in}}(t_1)\theta(t_2 - t_1), \tag{4.4}$$

with $\theta(x) = 1$ for $x > 0$ and $\theta(x) = 0$ for $x \leq 0$. The first term in this expression is only non-zero for times $t_1 > t_2$. For these times the commutator between the two currents, as given in Eq. (4.3), vanishes. Therefore, we can commute the two operators and combine both terms to arrive at

$$\mathcal{T} I_{\text{in}}(t_1) I_{\text{out}}(t_2) = I_{\text{out}}(t_2) I_{\text{in}}(t_1). \tag{4.5}$$

The same logic gives rise to the identities

$$\begin{aligned} \mathcal{T} I_{\text{out}}(t_1) I_{\text{out}}(t_2) &= I_{\text{out}}(t_1) I_{\text{out}}(t_2), \\ \mathcal{T} I_{\text{in}}(t_1) I_{\text{in}}(t_2) &= I_{\text{in}}(t_1) I_{\text{in}}(t_2), \\ \mathcal{T} I_{\text{out}}(t_1) I_{\text{in}}(t_2) &= I_{\text{out}}(t_1) I_{\text{in}}(t_2). \end{aligned} \tag{4.6}$$

As the commutator of in-in or out-out current products vanishes, the operator ordering in such pairs can be chosen as one prefers. With the given identities one concludes that time-ordering is equivalent to an ordering where all outgoing currents I_{out} are moved to the left and all incoming current I_{in} to the right [18]. In that way also the notation reflects causality, having the incoming current operator acting first on the state vector. For anti-time-ordering the whole formalism works similar but just by having the out-currents ordered to the right and the in-currents ordered to the left. We refer to the whole procedure by 'in-out ordering'´.

With the given formalism, we can decompose the $\mathcal{T}_C$ ordering into the action of moving all I^- to the left, all I^+ to the right and then doing the correct in-out ordering among the groups. It is important to recognize that this ordering does not depend on any of the time arguments of the currents. Going back to Eq. (4.1) and Eq. (4.2), the cumulant expressions we started from, we now have a simple procedure to connect these. We express the time dependent currents in their Fourier representation $I(t) = \int \frac{d\omega}{2\pi} I(\omega) e^{-i\omega t}$ so that Eq. (4.1) can be written as

$$\begin{aligned} C_n(t_1, t_2 ... t_n) &= \int \frac{d\omega_1}{2\pi} ... \int \frac{d\omega_n}{2\pi} \, \langle\langle \mathcal{T}_C I^{\alpha_1}(\omega_1) ... I^{\alpha_n}(\omega_n) \rangle\rangle e^{-i\omega_1 t_1} ... e^{-i\omega_n t_n} \\ &= \int \frac{d\omega_1}{2\pi} ... \int \frac{d\omega_n}{2\pi} \, C_n(\omega_1 ... \omega_n) e^{-i\omega_1 t_1} ... e^{-i\omega_n t_n} \end{aligned} \tag{4.7}$$

In frequency space, we can still easily apply the $\mathcal{T}_C$-ordering, using the in-out formalism. For the calculation of photon photon correlation functions in the following, we have to deal with operators expressed in frequency space and therefore it is more convenient to directly calculate the cumulants in frequency space. This can be achieved in a straight forwardly with the presented in-out formalism.

4.2 Diagrammatic Cumulant Calculation

Now, with the correct time-ordering and Wick's theorem, we can calculate any orders of current cumulants in principle. In this work, we restrict ourselves on the calculation up to and including the 4th order. The latter includes four current operators where each of them is a product of two fermionic operators. Thus, we have to calculate an expectation value with eight fermionic operators. With Wick's theorem we get $(2n-1)!!$ terms in general, where n is the number of current operators in the expression. These are 105 combinations for $n = 4$. However, as only creation operators paired with annihilation operators give non-zero results, we expect the number of finite terms to be at most $n!$, which is just 24 for $n = 4$. This number has to be multiplied by the number of different terms produced by the in-out ordering process and terms brought in by the different scattering matrix coefficients. Thus, going beyond the 4th-order current cumulant will be very complex. We proceed in different steps: First we calculate all in-out ordered terms of the involved current operators. Then we use Wick's theorem on every single term so that we have to evaluate only expectation values of pairs of creation and annihilation operators. At last, we evaluate these by using Eq. (3.1) and Eq. (3.2). To give this process more structure, we present a diagrammatic approach. First we give the diagrammatic rules and then calculate the first three orders of irreducible current cumulants. A 4th-order cumulant will be presented approximately.

Here we first explain how one has to translate an expression like

$$\langle\langle I^{\eta_1}(\omega_1) I^{\eta_2}(\omega_2) ... I^{\eta_n}(\omega_n) \rangle\rangle \tag{4.8}$$

into diagrams. The aim is to have graphical expressions that capture all important features of the mathematical counterparts. For this purpose, we represent

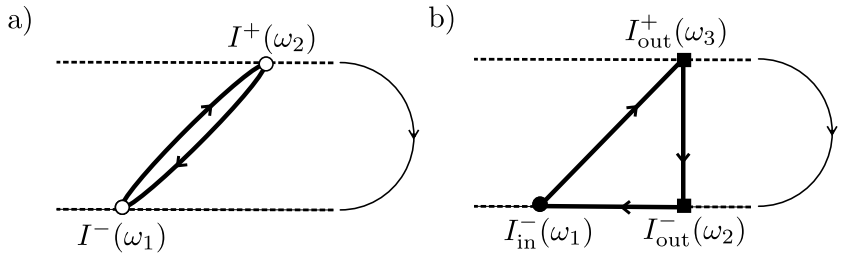

Figure 4.1: Simple diagram examples. In a) we show an example for the cumulant expression $\langle\langle \mathcal{T}_C I^-(\omega_1) I^+(\omega_2)\rangle\rangle$. The currents are represented by white empty circles. The small arrows on the thicker lines indicate the direction of the diagram (For two operator cumulants there is only one direction). The dashed line depicts the time axis, where the upper line corresponds to the forward Keldysh contour while the lower line corresponds to the backward contour. Minus currents are always drawn on the lower line, while plus currents are always drawn on the upper line. Following the line as suggested by the arrow on the right reflects the operator ordering in the cumulant. In the following, we cease to draw the connection between the forward and backward contour. A diagram containing full currents (empty white circles) corresponds to a sum over all in-out ordered subdiagrams with the given structure. In b) we show one of the directed diagrams representing the in-out ordered subdiagram $\langle\langle I^-_{\rm in}(\omega_1) I^-_{\rm out}(\omega_2) I^+_{\rm out}(\omega_3)\rangle\rangle$. Black filled circles correspond to in-currents while black squares denote out-currents. Incoming currents are always placed to the left of outgoing currents, implementing the Keldysh ordering into the diagrams.

every current in the cumulant by an empty white circle. The horizontal axis of the diagram represents the time axis, which we draw as a dashed line in the upper half, denoting the forward Keldysh contour and a dashed line in the lower half, denoting the backward Keldysh contour. These two Keldysh contours correspond to the time-ordering (forward contour) and the anti-time-ordering (backward contour) introduced in Section 4.1. The circles corresponding to the minus current operators live on the backward Keldysh contour and are consequently moved to the lower half, while the plus operators live on the forward contour and are drawn in the upper half. Now each circle corresponding to a current operator has to be connected with other current circles by two directed lines. One of these lines has to be incoming, while the other one has to be outgoing. An outgoing line depicts the pairing of a creation operator of the starting current with an annihilation operator of the current where the line ends. For irreducible cumulants, there must only be one closed loop including all current operators. To represent a complete cumulant, we have to sum over all possible topological different combinations of the above mentioned diagrams. This sum is then equivalent to all terms given by Wick's theorem.

Now every of these diagrams has to be split into in-out ordered subdiagrams. Each mother diagram then denotes the sum over all combinations of subdiagrams. In such, we depict incoming currents with dots and outgoing currents

with squares. In-currents are always placed left to out-currents on their respective contour. This way, the structure of the diagram corresponds to the order of operators in the cumulant, when following the Keldysh contour as indicated in Figure 4.1. Now we need rules to translate these diagrams into mathematical expressions. In this chapter we only present and use these rules, for a complete derivation see Appendix B.

We assume an energy independent scattering matrix for all calculations from this point. As already stated above, using the in-out ordering formalism leaves us with the correct physical ordering even if we drop the strict causality of the scattering matrix. Given these assumptions, we use the form of the scattering matrix in Eq. (3.12) and thus the outgoing current as given in (3.13). In this approximation and with the correct time-ordering already proceeded, we can calculate the in-out ordered subdiagrams by applying the following rules:

1. Every line in a diagram corresponds to either an f- or g- function as defined in Eq. (3.1) and Eq. (3.2). Whenever a line points against the direction of the Keldysh contour, it corresponds to the Fermi function $\langle c^\dagger_{\alpha,x} c_{\alpha,x}\rangle = f_\alpha(x)$. Lines pointing the other way around represent $\langle c_{\alpha,x} c^\dagger_{\alpha,x}\rangle = g_\alpha(x)$. The full diagram is then a product of the functions evaluated for every line.

2. For every line connecting two out-currents, sum over the resulting Fermi function's index α and multiply the corresponding term by either R for $\alpha = r$ or with T for $\alpha = l$. For a line going from an in-current to an out-current, $\alpha = r$ is fixed. Additionally, multiply by a factor of R. For a line that connects two in-currents or runs from an out-current to an in-current $\alpha = r$ is also fixed, but without an additional factor.

3. Evaluate the frequency argument of an f- or g-function by $\varepsilon + \bar{\omega}_i$, where $\bar{\omega}_i = \sum_{C_{ir}} \eta_j \omega_j$ is the sum over all frequencies of currents $I(\omega_j)$ along the contour C_{ir}. The contour C_{ir} is defined by the directed diagram lines, starting from an initial current $I(\omega_i)$ and ending at a reference current $I(\omega_r)$. Choose a fixed reference current for a diagram (for example the last current on the Keldysh contour). The initial current is the current, from which the line corresponding to the evaluated f- or g-function starts. The contour C_{ir} includes the frequency of the current where the contour ends and excludes the frequency of the current where it starts. As indicated by η_j, each frequency in $\bar{\omega}_i$ comes with a plus or minus sign, which is determined by the type of current (minus or plus current).

4. The sign of each diagram is given by $(-1)^{n_f+1}$, where n_f is the number of f-functions in the expression.

5. The expression contains a Dirac delta distribution of all contributing frequencies $\delta(\sum \eta_i \omega_i)$. For minus currents the frequency in the sum is subtracted, while for plus currents the corresponding frequency is added, as indicated by η_i.

6. Evaluate the integral $\int d\varepsilon$ over the full expression.

7. Perform a sum $\sum_m$ where m labels the different reflection and transmission probabilities R_m and T_m of different transverse modes.

These rules provide a simple recipe for the calculation of arbitrary current cumulants in the Landauer Büttiker formalism.

With the delta distribution in every term given by Rule 5, we define

$$C^{(n)}_{\eta_1\ldots\eta_n}(\omega_1,\omega_2\ldots\omega_n) = S^{(n)}_{\eta_1\ldots\eta_n}(\omega_1,\omega_2\ldots\omega_{n-1})\delta\big(\sum \eta_i\omega_i\big). \tag{4.9}$$

This way, we can treat the most interesting part of each cumulant $S^{(n)}_{\eta_1\ldots\eta_n}$ without the delta distribution. In $S^{(n)}_{\eta_1\ldots\eta_n}$, we always suppress the last frequency argument, which can be expressed by the other frequencies as related by the delta distribution. From now on, we also suppress the Keldysh ordering operator $\mathcal{T}_C$. Whenever we write a current operator I^η, we implicitly include the need to do a correct ordering according to η.

4.3 Analysis of the f- and g-Function Terms

In this section, we present properties of the f- and g-Fermi functions leading to useful transformations or approximations. We also discuss different types of products of f- and g-functions which are helpful in later calculations. Additionally, we use symmetries of the diagrams to reduce the number of different contributing terms.

4.3.1 Substitutions

For every diagram, we have to perform an ε-integral, which allows us to do substitutions in single terms of the expression. These help a lot in compressing the calculated expressions without performing the ε integral explicitly. They are of course only valid under the integral sign. All of them are rather trivial shifts in the variable ε. The simplest substitution is a shift in the energy by some frequency $\varepsilon \mapsto \varepsilon + \omega_j$. With this transformation, we can shift the arguments of different terms. A second transformation, also just a shift in the energy variable, has stronger effects. By setting $\varepsilon \mapsto \mu_l/\hbar - \varepsilon$, we can transform g-functions of one lead to f-functions of the other. Explicitly it maps

$$\begin{aligned} f_r(\varepsilon+\omega) &\mapsto g_l(\varepsilon-\omega),\\ f_l(\varepsilon+\omega) &\mapsto g_r(\varepsilon-\omega),\\ \Delta(\varepsilon+\omega) &\mapsto \Delta(\varepsilon-\omega) \end{aligned} \tag{4.10}$$

and vice versa. The origin of this mapping can be easily understood from the definitions of the f- and g-functions. Consider for example $f_l(\varepsilon+\omega)$. Performing the substitution explicitly, we have

$$\begin{aligned} f_l(\varepsilon+\omega) = \frac{1}{e^{[\hbar(\varepsilon+\omega)-\mu_l]/k_B\vartheta}+1} &\mapsto \frac{e^{\hbar(\varepsilon-\omega)/k_B\vartheta}}{e^{\hbar(\varepsilon-\omega)/k_B\vartheta}+1}\\ &= 1-\frac{1}{e^{\hbar(\varepsilon+\omega)/k_B\vartheta}+1} = g_r(\varepsilon-\omega) \end{aligned} \tag{4.11}$$

and similar for $f_r(\varepsilon+\omega)$. The third identity for $\Delta(\varepsilon+\omega)$ then directly follows from the first two. The presented transformation shows again that there is no difference in calculating with left or right currents. Diagrammatically the mapping changes the direction of a diagram and exchanges the right and left labels on the f- and g-functions. As we have to calculate both directions of every diagram, the change in direction does not affect the result. Thus, we see the equivalence between the results obtained by right or left currents. Another quiet similar mapping is given by substituting $\varepsilon \mapsto \varepsilon - \mu_l/\hbar$. It transforms left-labeled functions directly into right-labeled functions without changing the argument:

$$\begin{aligned} f_l(\varepsilon+\omega) &\mapsto f_r(\varepsilon+\omega), \\ g_l(\varepsilon+\omega) &\mapsto g_r(\varepsilon+\omega). \end{aligned} \tag{4.12}$$

However, the same substitution does not work in both directions. Using it on right-labeled functions only adds up the chemical potential, so that the new function does not correspond to the f- or g-functions we have defined. To change right-labeled functions into left-labeled functions, one has to use instead $\varepsilon \mapsto \varepsilon + \mu_l/\hbar$. Therefore, this mapping is mostly useful on terms that contain products of either only right- or only left-labeled functions.

4.3.2 Properties of f- and g-Functions

During the calculation of the diagrams, we are confronted with different types of products between f- and g-Fermi functions. Here, we first analyze two-function products, which occur in all cumulant terms. As we are especially interested in low temperature limits later, the best starting point for such an analysis is at $\vartheta = 0$. In this limit, all f- and g-functions turn into Heaviside theta functions with

$$\begin{aligned} f_\alpha(\varepsilon+\omega) &\mapsto \theta[(\mu_\alpha/\hbar-\omega)-\varepsilon], \\ g_\alpha(\varepsilon+\omega) &\mapsto \theta[\varepsilon-(\mu_\alpha/\hbar-\omega)]. \end{aligned} \tag{4.13}$$

Therefore, f_α is only non-zero for $\varepsilon < (\mu_\alpha/\hbar - \omega)$, while g_α has only finite contributions for $\varepsilon > [\mu_\alpha/\hbar - \omega]$. An interesting type of product is

$$f_l(\varepsilon) g_r(\varepsilon-\omega). \tag{4.14}$$

In the zero temperature limit, the g_r-function starts to be finite (for $\omega = 0$) at $\varepsilon = \mu_r/\hbar = 0$, while the f-function stops to be finite at $\varepsilon = \mu_l/\hbar = eV_0/\hbar$, so that the overlap is given by V_0. Even for $0 < \omega < eV_0/\hbar$ this term is still finite. These kind of products give the largest contributions compared to other possible product combinations. If the temperature raises, the f- and g-functions start to become smoother at the edge which makes the finite contribution even larger. The opposite behavior is found for the term

$$f_r(\varepsilon) g_l(\varepsilon-\omega). \tag{4.15}$$

The right Fermi function $f_r(\varepsilon)$ is already zero for $\varepsilon > 0$, while $g_l(\varepsilon + \omega)$ starts to be finite at V_0 (for $\omega = 0$) so that their product is zero for every ε. Even if the temperature rises, the tails of the Fermi functions have to be approximately as large as the bias voltage V_0 to create a finite overlap. Therefore, these terms can be classified as exponentially small in ϑ. For $\omega > 0$, the ending point of the f-function (so that it is zero for larger values) and the starting-point of the g-function (so that it is zero for smaller values) are pushed away from each other even further. There will be a finite overlap only for values $\omega < (-V_0)$. Analyzing the products

$$\begin{aligned} &f_l(\varepsilon)g_l(\varepsilon - \omega), \\ &f_r(\varepsilon)g_r(\varepsilon - \omega), \end{aligned} \tag{4.16}$$

we recognize that these also have to vanish for $\vartheta = 0$ and $\omega = 0$, because the g-function starts to be finite exactly at the point in the ε-space, where the f-function starts to be zero. A rising temperature also creates a finite overlap. However, because the edges of the Fermi functions are (for $\omega = 0$) located right next to each other, the overlap will grow faster than for the exponentially small terms and such products can be classified as polynomial in ϑ. For $\omega > 0$ such products also vanish (for zero temperature) and become finite for $\omega < 0$.

Above, we often mention the constraint $\omega \geq 0$. In the next chapter of this work, we model a detector that only responds to positive frequencies. There, we always fulfill this constraint. When we evaluate a diagram at zero temperature in this situation, we can neglect all terms containing products like Eq. (4.16) and Eq. (4.15). It turns out that under these circumstances solely in-out ordered diagrams with only out-currents are non-zero. Thus in such a case, we exclusively need to take only-out-current orderings into account [19]. We can then also rewrite Eq. (4.14) in the form

$$\begin{aligned} f_l(\varepsilon)g_r(\varepsilon - \omega) =& \Delta(\varepsilon)\Delta(\varepsilon - \omega) \\ =& f_l(\varepsilon)g_r(\varepsilon - \omega) + f_r(\varepsilon)g_l(\varepsilon - \omega) \\ &- f_l(\varepsilon)g_l(\varepsilon - \omega) - f_r(\varepsilon)g_r(\varepsilon - \omega). \end{aligned} \tag{4.17}$$

All the terms which are different on the left-hand side compared to the right-hand side vanish for $\vartheta = 0$. Even for small finite temperatures with $\vartheta \ll eV_0/k_B$, the zero temperature results can be good approximations for the physics, because non of the additional terms are exponential growing in the temperature. If the constraint of $\omega \geq 0$ is not given, one can still use the properties of the f- and g-functions stated above to constrain the frequency regime where one has to expect finite results.

4.3.3 Diagram Mappings

The mappings in Subsection 4.3.1 can be used to further simplify the expressions in some of the diagrams. It is useful to note that, whenever we have a diagram line evaluated as an f-function in one direction, it will be evaluated a g-function, with the same labels and negative frequency arguments ω_i, in the

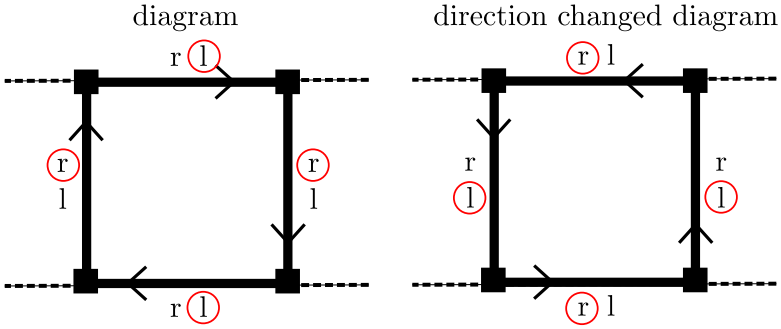

Figure 4.2: Two diagrams with four outgoing currents. The right diagram is the backward direction of the left diagram, as indicated by the arrows. In such diagrams with only out-currents, there is a sum over the side label for every line, which is here represented by the r l labels. Thus, we find every left-right combination so that there is always a labels exchanged term in the direction changed diagram. The red circles around the labels indicate such partner terms. If we considering the lines as chosen by the red circles in the left diagram, the choice in the right diagram corresponds to the partner term. The latter can be mapped onto the first term by using (4.10), as explained in the main text.

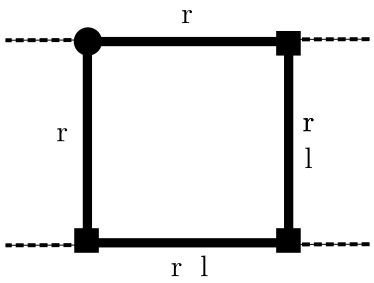

Figure 4.3: This figure shows a diagram with one incoming and three outgoing currents. The lines starting from and ending in the in-current are fixed to be right-labeled as indicated by the label r. The lines connecting two out currents correspond to a sum of a left and a right Fermi function indicated by the label r l. Since two lines are already fixed, we cannot find a direct labels-exchanged partner term.

other direction. This way, it is easy to calculate both directions of a diagram. Furthermore, we can use this property, together with a frequency shift and the mapping Eq. (4.10), to map terms of one diagram direction onto terms of the other direction, as explained in the following. Using the transformation Eq. (4.10), we turn f-functions into g-functions (and vice versa) with a sign-change of the frequencies and an exchange of the left and right labels. We see that changing the diagram direction or using the mapping Eq. (4.10) is identical up to the exchange of right and left labels. If we can identify two terms where one is the diagram direction changed term of the other, with additionally having right and left labels exchanged, we can use the mapping (4.10) on one of them. This renders the terms identical except from their prefactor. This trick is especially useful for diagrams containing only out-currents. In such a case all possible combinations of left and right labels occur so that every direction changed term has its partner term, as illustrated in Figure 4.2. However, the situation changes, when we have less out-currents. With only one out-current gone, two lines are fixed to be right-labeled (no sum over the label), as indicated in Figure 4.3. Therefore, we can only find labels-exchanged partner terms for fully out-current contributions.

Nevertheless, for all terms containing either only left- or only right-labeled functions, one can use mapping Eq. (4.12) on top of mapping Eq. (4.10). We already stated that changing the diagram direction and using the first substitution is equivalent up to the exchange of the labels. The second substitution then also exchanges the labels back so that such terms always map on their direct direction-changed terms (no label exchanged partner term needed), except from a possible sign-change caused by a different number of f-functions in the original term. For odd-order cumulants, the direction changed term has always a minus-sign relative to it's original term because the number of f-functions changes from even to odd. From the fact of having this minus sign and the mapping between only left-labeled and only right-labeled terms, it follows that such terms always cancel each other. If we deal with even-order cumulants, this minus sign does not occur because both directions of a diagram contain the same number of f-functions. Thus, we do not find a direct cancellation between the two directions of only left-labeled or only right-labeled terms. Nevertheless, for the 4th-order we checked numerically that after the ε-integration those terms in sum also vanish. Therefore, we can always neglect such terms in odd-order cumulants and at least in the 4th-order cumulant.

4.4 Example Calculations

In this section, we use the presented rules to calculate different examples. We present only current irreducible cumulants, from which one can construct results for other quantities depending on currents. We only consider one transverse current mode m for simplicity. However, all results are also valid for many mode setups if summing over the index m of the reflection and transmission coefficients R_m and T_m. For the purpose of giving a better overview, we list all results obtained in this section again in Appendix C.

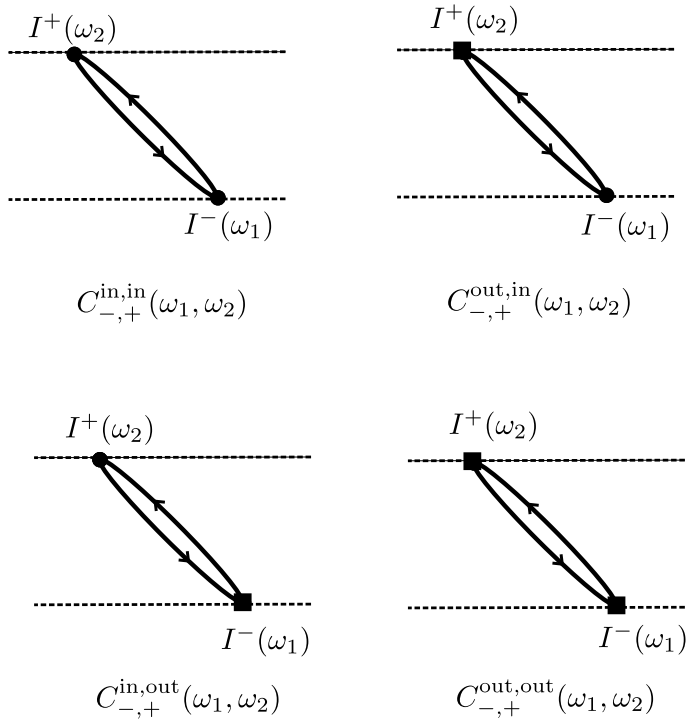

Figure 4.4: All subdiagrams contributing to $C^{(2)}_{-+}(\omega_1,\omega_2) = S^{(2)}_{-+}(\omega_1)\delta(\omega_2-\omega_1)$. There is only a single diagram topology possible with two current operators. Therefore, the different subdiagrams simply correspond to the different in-out orderings. The diagrams including one or two in-currents result in only one term, because the corresponding lines are fixed to be right-labeled by the in current. However, the out,out-diagram contributes four terms because every line brings in a sum over right- and left-labeled functions.

4.4.1 First-Order Cumulant

The first-order irreducible cumulant is equivalent to the mean current flowing. It is simply given by

$$C^{(1)}_{\pm}(\omega_1) = \langle I^{\pm}\rangle = I_0\delta(\omega_1), \tag{4.18}$$

where I_0 is the net current through the QPC. From the delta distribution $\delta(\omega_1)$, we see that the mean current is given by a zero frequency current without any finite frequency contributions.

4.4.2 Second-Order Cumulant

While the first-order cumulant corresponds to the mean current, higher orders give rise to quantum mechanical current fluctuations. Here, we compute different irreducible second-order cumulants in frequency space. Beginning with

$$C^{(2)}_{-+} = \langle\langle I^-(\omega_1)I^+(\omega_2)\rangle\rangle, \tag{4.19}$$

we are going to do the correct Keldysh ordering first. This task is a very simple step here because we have only two current operators where one of them is a minus current and the other one a plus current. Therefore, the in-out ordering process reduces to splitting the currents into in- and out-currents. We obtain

$$\begin{aligned} S^{(2)}_{-+}(\omega_1)\delta(\omega_2-\omega_1) =& \langle\langle I^-_{\text{in}}(\omega_1) I^+_{\text{in}}(\omega_2)\rangle\rangle - \langle\langle I^-_{\text{in}}(\omega_1) I^+_{\text{out}}(\omega_2)\rangle\rangle \\ & - \langle\langle I^-_{\text{out}}(\omega_1) I^+_{\text{int}}(\omega_2)\rangle\rangle + \langle\langle I^-_{\text{out}}(\omega_1) I^+_{\text{out}}(\omega_2)\rangle\rangle. \end{aligned} \tag{4.20}$$

These terms can be represented as the diagrams given in Figure 4.4. With $S^{ii}_{-+}(\omega_1,\omega_2)$, we denote the term containing two in-currents with the frequency arguments in the given order and similar for other current combinations. Now we can evaluate the term and receive

$$S^{ii}_{-+}(\omega_1,\omega_2) = \int d\varepsilon\; f_r(\varepsilon) g_r(\varepsilon-\omega_1). \tag{4.21}$$

The Fermi function representing the first line $f_r(\varepsilon)$ has no ω-frequency argument because we chose the last current on the backward contour (lower left corner of the diagram) as the reference current. We point out that for two-current cumulants only one direction of the diagrams occurs because two operators can only be paired in one way. For the other orderings, we can proceed the same way and end up with

$$S^{io}_{-+}(\omega_1,\omega_2) = S^{oi}_{-+}(\omega_1,\omega_2) = R\int d\varepsilon\; f_r(\varepsilon) g_r(\varepsilon-\omega_1). \tag{4.22}$$

Only for $S^{oo}_{-+}(\omega_1,\omega_2)$, we find an expression containing more than one term, which is given by

$$\begin{aligned} S^{oo}_{-+}(\omega_1,\omega_2) = \int d\varepsilon \Big\{ & R^2 f_r(\varepsilon) g_r(\varepsilon-\omega_1) + T^2 f_l(\varepsilon) g_l(\varepsilon-\omega_1) \\ & + RT\big[f_r(\varepsilon) g_l(\varepsilon-\omega_1) + f_l(\varepsilon) g_r(\varepsilon-\omega_1)\big]\Big\}. \end{aligned} \tag{4.23}$$

Here, we can make use of the presented substitutions in Subsection 4.3.1 to simplify the expression. We can map the term $f_l(\varepsilon)g_l(\varepsilon-\omega_1) \mapsto f_r(\varepsilon+\omega_1)g_r(\varepsilon)$ with Eq. (4.10) and then use a shift $\varepsilon \mapsto \varepsilon-\omega_1$, which maps $f_r(\varepsilon+\omega_1)g_r(\varepsilon) \mapsto f_r(\varepsilon)g_r(\varepsilon-\omega_1)$. Then, we can rewrite (4.23) as

$$\begin{aligned} S^{oo}_{-+}(\omega_1,\omega_2) = \int d\varepsilon \Big\{ & (1-2RT) f_r(\varepsilon) g_r(\varepsilon-\omega_1) \\ & + RT\big[f_r(\varepsilon) g_l(\varepsilon-\omega_1) + f_l(\varepsilon) g_r(\varepsilon-\omega_1)\big]\Big\}. \end{aligned} \tag{4.24}$$

Combining the four expressions properly leaves us with

$$S^{(2)}_{-,+}(\omega_1,\omega_2) = \int d\varepsilon \Big\{ RT\big[\Delta(\varepsilon)\Delta(\varepsilon-\omega_1)\big] + 2T\big[f_r(\varepsilon) g_r(\varepsilon-\omega_1)\big]\Big\}. \tag{4.25}$$

The second-order cumulant with only plus currents is calculated in the same straight forward way. Only the sign of ω_1 and the time-ordering for $S^{io}_{++}(\omega_1,\omega_2)$

compared to $S^{io}_{-+}(\omega_1,\omega_2)$ changes because in this case, we have to do the in-out ordering explicitly. We find

$$S^{(2)}_{++}(\omega_1,\omega_2) = \int d\varepsilon \Big\{ RT\big[\Delta(\varepsilon)\Delta(\varepsilon+\omega_1)\big] + Tf_r(\varepsilon)\big[g_r(\varepsilon+\omega_1)+g_r(\varepsilon-\omega_1)\big] + f_r(\varepsilon)\big[g_r(\varepsilon+\omega_1)-g_r(\varepsilon-\omega_1)\big]\Big\}. \tag{4.26}$$

The last two terms are symmetrized in the frequency arguments, which turns out to be typical for single-contour terms. The first term of both expressions vanishes for zero voltage bias because the difference Fermi-functions obey the property $\Delta(x) = 0$ for $V_0 = 0$, as explained in Chapter 3. The second term in contrast does not vanish for zero bias voltage but in the case of zero temperature (if $\omega > 0$). Hence, we refer to it with thermal-noise term. Only dealing with positive frequencies together with the analysis in Sec.(4.3.2) is sufficient for these terms to vanish. The same logic applies for left-labeled products $f_l(\varepsilon)g_l(\varepsilon-\omega_1)$.

When calculating all combinations of different cumulants for a given order, it is enough to calculate only one example for every combination determined solely by the number of current-plus signs. These examples can then be related to the other orderings. Finding the other orderings when the number of plus signs is kept invariant is quiet simple. For the second order, the plus minus switched cumulant $C^{(2)}_{+-}(\omega_1,\omega_2)$ is given by the non-switched term with the frequencies exchanged:

$$C^{(2)}_{+-}(\omega_1,\omega_2) = C^{(2)}_{-+}(\omega_2,\omega_1). \tag{4.27}$$

The reason for this is the Keldysh time-ordering that orders the plus and minus currents to the right and to the left anyway. However, this reordering then also exchanges the frequencies. To relate the $++$- with the $--$-cumulant, we use the property that adjugating a current operator negates its frequency argument. Additionally, we have to change a plus label to a minus label (and vice versa), giving rise to the relations $[I^+(\omega)]^\dagger = I^-(-\omega)$ and $[I^-(\omega)]^\dagger = I^+(-\omega)$. This takes care of the correct time-ordering, which turns from time-ordering into anti-time-ordering by adjugation. With this, we can derive the relation

$$\begin{aligned}[C^{(2)}_{++}(\omega_1,\omega_2)]^* &= \langle\langle [I^+(\omega_1)I^+(\omega_2)]^\dagger\rangle\rangle \\ &= \langle\langle [I^+(\omega_2)]^\dagger [I^+(\omega_1)]^\dagger\rangle\rangle \\ &= \langle\langle I^-(-\omega_2)I^-(-\omega_1)\rangle\rangle = C^{(2)}_{--}(-\omega_2,-\omega_1)\end{aligned} \tag{4.28}$$

from which we extract

$$[S^{(2)}_{++}(\omega_1)\delta(\omega_1+\omega_2)]^* = S^{(2)}_{--}(-\omega_2)\delta(\omega_1+\omega_2) = S^{(2)}_{--}(\omega_1)\delta(\omega_1+\omega_2) \tag{4.29}$$

so that $S^{(2)}_{--}(\omega_1) = [S^{(2)}_{++}(\omega_1)]^*$.

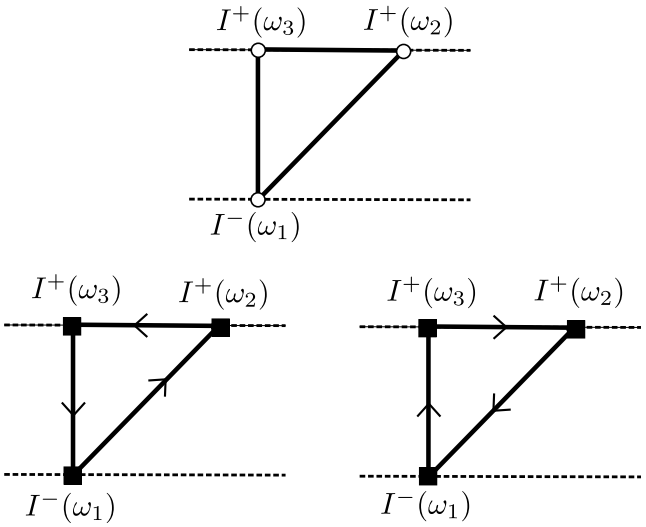

Figure 4.5: The upper diagram represents $C^{(3)}_{-++}(\omega_1, \omega_2, \omega_3)$. The diagram corresponds to the sum over all terms produced by applying the correct in-out ordering. The lower two diagrams are already in-out ordered subdiagrams with only out-currents. They represent the two possible directions of the diagram, as indicated by the little arrows.

4.4.3 Third-Order Cumulant

In this subsection, we present the results for the third-order cumulant. As an example, we calculate

$$C^{(3)}_{-++} = \langle\langle I^-(\omega_1) I^+(\omega_2) I^+(\omega_3)\rangle\rangle, \tag{4.30}$$

which is represented by the upper diagram in Figure 4.5. We have suppressed the frequency argument in $C^{(3)}_{-++}$ for convenience and will also do so for other quantities throughout this work. Whenever we proceed like this and the frequency arguments are not clear, we will give them separately. Here the in-out ordering is a little more complex than in the previous case. The current $I^-(\omega_1)$ will always stay in first position but the two operators $I^+(\omega_2)$ and $I^+(\omega_3)$ have to be ordered correctly. Proceeding with the ordering leads to

$$\begin{aligned} C^{(3)}_{-++} = {} & \langle\langle I^-_{\mathrm{in}}(\omega_1) I^+_{\mathrm{in}}(\omega_2) I^+_{\mathrm{in}}(\omega_3)\rangle\rangle - \langle\langle I^-_{\mathrm{in}}(\omega_1) I^+_{\mathrm{out}}(\omega_2) I^+_{\mathrm{in}}(\omega_3)\rangle\rangle \\ & - \langle\langle I^-_{\mathrm{in}}(\omega_1) I^+_{\mathrm{out}}(\omega_3) I^+_{\mathrm{in}}(\omega_2) + \langle\langle I^-_{\mathrm{in}}(\omega_1) I^+_{\mathrm{out}}(\omega_2) I^+_{\mathrm{out}}(\omega_3)\rangle\rangle \\ & - \langle\langle I^-_{\mathrm{out}}(\omega_1) I^+_{\mathrm{in}}(\omega_2) I^+_{\mathrm{in}}(\omega_3)\rangle\rangle + \langle\langle I^-_{\mathrm{out}}(\omega_1) I^+_{\mathrm{out}}(\omega_2) I^+_{\mathrm{in}}(\omega_3)\rangle\rangle \\ & + \langle\langle I^-_{\mathrm{out}}(\omega_1) I^+_{\mathrm{out}}(\omega_3) I^+_{\mathrm{in}}(\omega_2) - \langle\langle I^-_{\mathrm{out}}(\omega_1) I^+_{\mathrm{out}}(\omega_2) I^+_{\mathrm{out}}(\omega_3)\rangle\rangle. \end{aligned} \tag{4.31}$$

However, we can neglect all terms depending on products of either only left-labeled or only right-labeled functions because they cancel out as shown in Subsection 4.3.3. In-out ordered terms containing only one ore less out-currents consist solely of such one-sided terms and can therefore be completely neglected. Thus, we have to deal with only four different in-out orderings.

Here we show the calculation of the out,out,out-term explicitly. In contrast to the two-current example, every term contributes with two directions of the diagram as shown in the lower part of Figure 4.5. Using again the presented diagram rules, we find

$$S^{ooo}_{-++} = \int d\varepsilon \sum_{\alpha_1,\alpha_2,\alpha_3} s_{\alpha_1} s_{\alpha_2} s_{\alpha_3} \big[g_{\alpha_1}(\varepsilon) g_{\alpha_2}(\varepsilon+\omega_2) f_{\alpha_3}(\varepsilon+\omega_1) - f_{\alpha_1}(\varepsilon) f_{\alpha_2}(\varepsilon-\omega_2) g_{\alpha_3}(\varepsilon-\omega_1) \big], \tag{4.32}$$

where

$$s_\alpha = \begin{cases} R & \forall \alpha = r \\ T & \forall \alpha = l \end{cases}. \tag{4.33}$$

The fact that there are only out-currents in the expression is the origin of the sum over all three indexes. Having this sum present, it is very useful to use Eq. (4.10) to map the Fermi functions of the second term onto the first, as explained in 4.3.3. We find

$$S^{ooo}_{-++} = \int d\varepsilon \sum_{\alpha_1,\alpha_2,\alpha_3} (s_{\bar\alpha_1} s_{\bar\alpha_2} s_{\bar\alpha_3} - s_{\alpha_1} s_{\alpha_2} s_{\alpha_3}) \times f_{\alpha_1}(\varepsilon) f_{\alpha_2}(\varepsilon-\omega_2) g_{\alpha_3}(\varepsilon-\omega_1). \tag{4.34}$$

With $\bar\alpha_i$ we denote the opposite of α_i, for example if we have $\alpha_i = l$, then $\bar\alpha_i = r$. Ignoring the only-out-current and only-in-current terms (because they vanish), the prefactor $(s_{\bar\alpha_1} s_{\bar\alpha_2} s_{\bar\alpha_3} - s_{\alpha_1} s_{\alpha_2} s_{\alpha_3})$ can be evaluated as

$$(-1)^{\#l}(R^2T - RT^2) = (-1)^{\#l}(RT - 2RT^2), \tag{4.35}$$

where $\#l$ is the number of left labeled functions in the term. By reinserting the vanishing terms again, we can express this as

$$S^{ooo}_{-++}(\omega_1,\omega_2,\omega_3) = \int d\varepsilon \; (RT - 2RT^2)\Delta(\varepsilon)\Delta(\varepsilon-\omega_1)\Delta(\varepsilon-\omega_2). \tag{4.36}$$

Now, that we have calculated the out,out,out-expression, there are only three interesting in-out orderings left. For $S^{ioo}_{-++}(\omega_1,\omega_2,\omega_3)$ the in-out ordering is already correct from the beginning, while $S^{ooi}_{-++}(\omega_1,\omega_2,\omega_3)$ contributes once with the initial order and once as $S^{ioo}_{-++}(\omega_1,\omega_3,\omega_2)$ with the second and third current swapped. All of these terms are proportional to RT. The two orderings for which the frequency arguments are the same as in S^{ooo}_{-++} also occur in S^{ooo}_{-++}. However, these terms have different signs because the first two origin from out,out,in-terms while the latter are part of an out,out,out-term. Thus, these terms cancel each other. By adding the left-over term $S^{ioo}_{-++}(\omega_1,\omega_3,\omega_2)$ to the rest of the out,out,out-RT terms, we find the full third-order current cumulant in frequency space to be

$$S^{(3)}_{-++}(\omega_1,\omega_2,\omega_3) = \int d\varepsilon \; \big\{ -2RT^2\Delta(\varepsilon)\Delta(\varepsilon-\omega_1)\Delta(\varepsilon-\omega_2) + RT\big[f_l(\varepsilon) g_r(\varepsilon-\omega_1) - f_r(\varepsilon) g_l(\varepsilon-\omega_1) \big] \big\}. \tag{4.37}$$

For the calculation of $S^{(3)}_{+++}$, the only out-current term does not change compared to the $-++$-case, except from the sign of ω_1. However, some of the terms with incoming currents have a different in-out ordering because in the $+++$-case, all currents are on the same Keldysh contour. This way, in contrast to the calculation of $S^{(3)}_{-++}$, the in-out ordering takes place among all three currents. The final result writes

$$\begin{aligned} S^{(3)}_{+++}(\omega_1,\omega_2,\omega_3) = \int d\varepsilon\, \big\{ & -2RT^2\Delta(\varepsilon)\Delta(\varepsilon+\omega_1)\Delta(\varepsilon-\omega_2) \\ & + RTf_l(\varepsilon)\big[f_r(\varepsilon+\omega_2)g_l(\varepsilon-\omega_1) - f_r(\varepsilon-\omega_2)g_l(\varepsilon+\omega_1)\big] \\ & + RTf_r(\varepsilon)\big[f_l(\varepsilon-\omega_2)g_r(\varepsilon+\omega_1) - f_l(\varepsilon+\omega_2)g_r(\varepsilon-\omega_1)\big] \\ & + RT\big[f_l(\varepsilon)g_r(\varepsilon+\omega_1) - f_r(\varepsilon)g_l(\varepsilon+\omega_1)\big]\big\}. \end{aligned} \tag{4.38}$$

Compared to the $-++$-version, we find two additional terms. If the voltage difference between the left and right reservoirs is tuned to zero, both cumulants vanish. In contrast to the second order, there is no purely thermal contribution.

To find the other combinations of plus-minus cumulants, we can use the relations that we give below. If the number of plus signs does not change, the Keldysh ordering maps the first term on the second one, except from a change of the frequencies, similar to 4.4.2. This gives rise to

$$C^{(3)}_{-++}(\omega_1,\omega_2,\omega_3) = C^{(3)}_{++-}(\omega_3,\omega_2,\omega_1) = C^{(3)}_{+-+}(\omega_2,\omega_1,\omega_3), \tag{4.39}$$

implying

$$\begin{aligned} S_{++-}(\omega_1,\omega_2) &= S_{-++}(\omega_1-\omega_2,\omega_2), \\ S_{+-+}(\omega_1,\omega_2) &= S_{-++}(\omega_2,\omega_1). \end{aligned} \tag{4.40}$$

Analogous to the second-order calculations, we can derive another set of relations that links third-order cumulants that have different numbers of plus signs. As a first relation, we have

$$\begin{aligned} [C^{(3)}_{-++}(\omega_1,\omega_2,\omega_3)]^* &= \langle\langle [I^-(\omega_1)I^+(\omega_2)I^+(\omega_3)]^\dagger\rangle\rangle \\ &= \langle\langle [I^+(\omega_3)]^\dagger [I^+(\omega_2)]^\dagger [I^-(\omega_1)]^\dagger\rangle\rangle \\ &= \langle\langle I^-(-\omega_3)I^-(-\omega_2)I^+(-\omega_1)\rangle\rangle \\ &= C^{(3)}_{--+}(-\omega_3,-\omega_2,-\omega_1), \end{aligned} \tag{4.41}$$

which implies

$$S^{(3)}_{--+}(\omega_1,\omega_2) = [S^{(3)}_{-++}(\omega_2-\omega_1,-\omega_2)]^*. \tag{4.42}$$

In the same way, we find

$$C^{(3)}_{---}(\omega_1,\omega_2,\omega_3) = [C^{(3)}_{+++}(-\omega_3,-\omega_2,-\omega_1)]^* \tag{4.43}$$

and therefore

$$S^{(3)}_{---}(\omega_1,\omega_2) = [S^{(3)}_{+++}(\omega_1+\omega_2,\omega_2)]^*. \tag{4.44}$$

With all the relations above and the two results (4.37) and (4.38), one has all possible combinations for third-order current cumulants at hand.

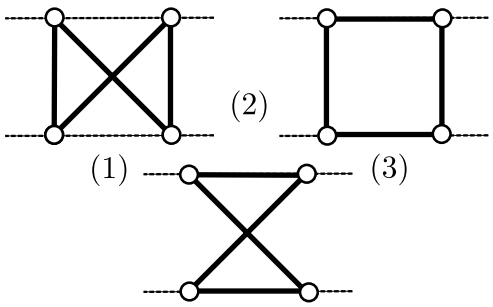

Figure 4.6: All diagrams contributing to the current irreducible 4th-order cumulant. The labeling of the currents follows the same structure as for the preceding diagrams. Therefore, we suppress the current and frequency labels whenever it follows, like here, the standard scheme. For the 4th order, we have more than one possible diagram topology. The first diagram occupies the largest frequency space because it has no connection between currents on the same contour. As frequencies on the same contour in the Fermi functions have the same sign, they add up and suppress the whole term. This is explained more detailed in the main text.

4.4.4 4th-Order Cumulant

We were able to produce quiet compact results for the third-order cumulants and lower. However, for the 4th-order this is more complicated. Therefore, we calculate only the cumulant that we need for the calculation in the next chapter. For this purpose, we add an additional feature to the plus and minus currents and calculate only at $\vartheta = 0$. Every current now carries a theta function with the current frequency as an argument, giving rise to

$$I^{\pm}(\omega) = 0 \ \ \forall \ \ \omega \leq 0. \tag{4.45}$$

This corresponds to currents only emitting photons, which then produce a signal in a detector based on absorption. Now we can use the constrain $\omega_i > 0$ for all frequencies. The zero frequency part does not play a role for irreducible cumulants with order greater than one, because they do not contain delta distributions of single frequencies. Before we start with the calculation, it is probably useful to mention that with the positive choice of frequencies, all diagrams which consist solely of plus or solely minus currents are always zero. A diagram that lives only on one of the contour branches is equivalent to a cumulant with either only minus or only plus currents. As given by 4.2 Rule 5, there is a Dirac delta distribution $\delta(\sum_i \eta_i \omega_i)$ in every term. For a diagram containing only minus currents, we have all $\eta_i = -1$, while for only plus currents, we have $\eta_i = 1$. As all frequencies are strictly positive, this delta distribution is always zero, rendering the full term zero.

The 4th-order cumulant that we are going to need in the Chapter 5 is the minus-plus symmetric

$$C^{(4)}_{--++} = \langle\langle I^-(\omega_1) I^-(\omega_2) I^+(\omega_3) I^+(\omega_4)\rangle\rangle. \tag{4.46}$$

The in-out ordering process is as straight forward as for the smaller order cumulants but produces 16 terms. For this reason, we do not write down all orderings here. However, one can again neglect all terms containing only left- and only right-labeled functions so that all terms with less than two out-currents vanish. But not only the number of orderings increases compared to the third-order cumulant, the whole expression will be a lot more involved. Yet, the recipe for the calculation given in the previous examples still works. As we only compute results for $\vartheta = 0$, we exclusively need to take the out,out,out,out-ordering into account, as explained in Section 4.3.2.

First we select the contributing diagrams. The full 4th-order irreducible cumulant can be represented by the three different directed diagrams shown in Figure 4.6. Already before proceeding with the full calculation, we see that the diagram (1) occupies the largest frequency space. The other two diagrams have lines that connect two currents on the same branch of the Keldysh contour. Thus, those contractions depend on a sum of frequencies from the same contour branch. Originating from the same branch, these frequencies are both either positive or negative. Therefore, they add up and suppress those terms in the sense of pushing the ending point of f- and the starting point of g-functions further away from each other, as explained in Section 4.3.2. In diagram (1) however, we always connect a positive with a negative frequency current, keeping the suppression lower. We can do similar steps as for the calculation of S^{ooo}_{-++} and get the three contributions

$$\begin{aligned}
S^{oooo}_{1--++} &= -\int d\varepsilon \sum_{\alpha_1,\alpha_2,\alpha_3,\alpha_4} (s_{\bar{\alpha}_1} s_{\bar{\alpha}_2} s_{\bar{\alpha}_3} s_{\bar{\alpha}_4} + s_{\alpha_1} s_{\alpha_2} s_{\alpha_3} s_{\alpha_4}) \\
&\qquad \times f_{\alpha_1}(\varepsilon) g_{\alpha_2}(\varepsilon - \omega_4) f_{\alpha_3}(\varepsilon + \omega_2 - \omega_4) g_{\alpha_4}(\varepsilon - \omega_1), \\
S^{oooo}_{2--++} &= -\int d\varepsilon \sum_{\alpha_1,\alpha_2,\alpha_3,\alpha_4} (s_{\bar{\alpha}_1} s_{\bar{\alpha}_2} s_{\bar{\alpha}_3} s_{\bar{\alpha}_4} + s_{\alpha_1} s_{\alpha_2} s_{\alpha_3} s_{\alpha_4}) \\
&\qquad \times f_{\alpha_1}(\varepsilon) f_{\alpha_2}(\varepsilon + \omega_2) g_{\alpha_3}(\varepsilon + \omega_2 - \omega_4) g_{\alpha_4}(\varepsilon - \omega_1), \\
S^{oooo}_{3--++} &= \int d\varepsilon \sum_{\alpha_1,\alpha_2,\alpha_3,\alpha_4} (s_{\bar{\alpha}_1} s_{\bar{\alpha}_2} s_{\bar{\alpha}_3} s_{\bar{\alpha}_4} + s_{\alpha_1} s_{\alpha_2} s_{\alpha_3} s_{\alpha_4}) \\
&\qquad \times f_{\alpha_1}(\varepsilon) f_{\alpha_2}(\varepsilon + \omega_2) f_{\alpha_3}(\varepsilon + \omega_2 - \omega_3) g_{\alpha_4}(\varepsilon - \omega_1),
\end{aligned} \tag{4.47}$$

corresponding to the diagrams (1), (2), and (3). For the $\vartheta = 0$ case, all terms containing a product of $f_r(\varepsilon) g_l(\varepsilon - \omega)$, $f_l(\varepsilon) g_l(\varepsilon - \omega)$ and $f_l(\varepsilon) g_l(\varepsilon - \omega)$ vanish. Every of the three terms above has only one term left after filtering out the vanishing terms. We end up with

$$\begin{aligned}
\tilde{S}^{oooo}_{1--++} &= -2R^2T^2 \int d\varepsilon \; f_l(\varepsilon) g_r(\varepsilon - \omega_4) f_l(\varepsilon + \omega_2 - \omega_4) g_r(\varepsilon - \omega_1), \\
\tilde{S}^{oooo}_{2--++} &= -2R^2T^2 \int d\varepsilon \; f_l(\varepsilon) f_l(\varepsilon + \omega_2) g_r(\varepsilon + \omega_2 - \omega_4) g_r(\varepsilon - \omega_1), \\
\tilde{S}^{oooo}_{3--++} &= (RT - 2R^2T^2) \int d\varepsilon \; f_l(\varepsilon) f_l(\varepsilon + \omega_2) f_l(\varepsilon + \omega_2 - \omega_3) g_r(\varepsilon - \omega_1),
\end{aligned} \tag{4.48}$$

where the tilde indicates that the quantities are evaluated at zero temperature. We write this into the form

$$\begin{aligned}
\tilde{S}^{oooo}_{1--++} &= -2R^2T^2 \int d\varepsilon\, d\varepsilon \Delta(\varepsilon)\Delta(\varepsilon-\omega_4)\Delta(\varepsilon+\omega_2-\omega_4)\Delta(\varepsilon-\omega_1),\\
\tilde{S}^{oooo}_{2--++} &= -2R^2T^2 \int d\varepsilon\, \Delta(\varepsilon)\Delta(\varepsilon+\omega_2)\Delta(\varepsilon+\omega_2-\omega_4)\Delta(\varepsilon-\omega_1),\\
\tilde{S}^{oooo}_{3--++} &= (RT-2R^2T^2) \int d\varepsilon\, \Delta(\varepsilon)\Delta(\varepsilon+\omega_2)\Delta(\varepsilon+\omega_2-\omega_3)\Delta(\varepsilon-\omega_1),
\end{aligned} \tag{4.49}$$

which is possible because all terms in this expression differing from (4.48) vanish for $\vartheta = 0$. When we now compare to the original term (4.47), it turns out that the terms proportional to R^2T^2 are actually exact in the form given by Eq. (4.49) even for finite temperatures. This is because R^2T^2 terms only occur in the four-out-current contribution in all possible Fermi function combinations. All this different combinations are contained in the terms given by (4.49) when it is expanded. For the terms proportional to RT and RT^2, we do not have all possible combinations and therefore add too many terms if expressing all Fermi functions by $\Delta(x)$. Additionally, there are corrections for those terms introduced by non-four-out-current contributions. All these corrections do not have large influence on the result for small temperatures. Thus, approximating the full cumulant by the terms above captures the main contribution to the 4th-order cumulant in a good approximation.

Chapter 5

Measurement of Non-Classical Radiation

We already explained in Chapter 2 that for coherent laser light or thermal radiation, photons occur in bunches. This leaves us with the question on how to measure the antibunching effect of photons. A general approach is to use the statistics of electrons, which do naturally antibunch because of the Pauli principle. Existing examples are single photon sources, where one single electron is excited and emits a photon when relaxing. However, the question rises if there is a quantum limit to the classical light bulb, producing antibunching radiation by a voltage biased wire. A possible answer has been given by Beenakker [19]. The idea is to use a quantum point contact biased at a potential V_0. The barrier in the point contact gives rise to fluctuations in the flowing currents that furthermore results in emitted photons. The full system has to be embedded in an electrical circuit, which modifies the allowed frequencies of the current and thus the photons. Low frequencies are suppressed in such a manner that photons are at most emitted at the frequency of the potential difference. Then, by energy conservation, the photon emitting electron cannot radiate a second photon. As an addition, only a single channel should be allowed to contribute to the current. Otherwise the non-classical properties can already be gone, as explained further below. Using this approach, quantities like the Fano factor and different cumulants for the photon counting statistics have already been calculated [6, 8, 19]. In contrast, we additionally calculate the time resolved $g^{(2)}(\tau)$, which contains also information about correlation time. In the following chapter, we first introduce the detailed setup. We then reproduce known results from the Fano factor and determine the critical temperature below which one can observe non-classical results for a QPC as a source of radiation. We furthermore calculate the time resolved quantity $g^{(2)}(\tau)$ for the described setup. From this, we will be able to determine a relaxed constraint on the critical temperature, giving a broader range of possible experimental parameters.

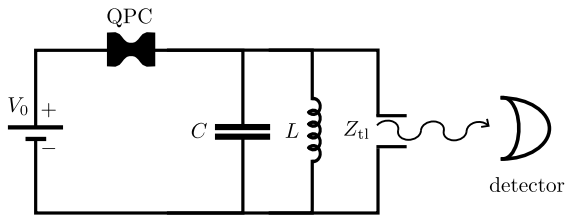

Figure 5.1: Setup of the system of interest. We study a quantum point contact biased by a voltage V_0 and embedded into an electrical environment. The environment consists of an LC-resonator with capacitance C and inductance L and a transmission line with impedance Z_{tl}. It prefers photons with a frequency in the vicinity of the resonance frequency of the resonator. Photons dissipated through the transmission line can be detected with a detector.

5.1 Setup

We study a quantum point contact (QPC) biased at voltage V_0, embedded in an electrical circuit, consisting of an LC-resonator and a transmission line in parallel. Photons radiated by the quantum point contact propagate through the transmission line and can then be detected. The LC resonator on it's own is characterized by the resonance frequency $\omega_0 = (LC)^{-1/2}$ and a characteristic impedance $Z_0 = (L/C)^{1/2}$. The latter is the ratio of the voltage and the current at the resonance frequency. We want the voltage bias over the quantum point contact to be constant, which can only be guaranteed for a small impedance of the LC-circuit plus transmission line. The impedance of the quantum point contact is given by $2\pi\hbar/e^2T$. This implies the inequality $G_Q Z_0 \ll 1$ with $G_Q = 2\pi\hbar/e^2$. We can divide our setup into a source, given by the QPC, and a detection part consisting of the LC-circuit and the transmission line. The transmission line introduces a damping and a slight shift in the resonance frequency of the resonator. This shift of the resonance frequency is not crucial here and can be included in a redefinition of ω_0. The important effect is the damping, which can be described by the real part of the transmission line impedance $Z_{\mathrm{tl}}(\omega \approx \omega_0) = Z_0\omega_0/\gamma$. The parameter γ can be shown to correspond to the rate of photon loss into the transmission line. The full impedance of the detection part is then given by

$$Z(\omega) = \frac{Z_0\omega\omega_0}{i(\omega_0^2 - \omega^2) + \gamma\omega}, \tag{5.1}$$

which simply results from adding up the inverse impedances of each element. It relates the current through the QPC with the voltage drop over the detection part $V(\omega) = Z(\omega)I(\omega)$. For positive frequencies (emission) and $\omega_0/\gamma \gg 1$, we can approximate this result with

$$\tilde{Z}(\omega) = \frac{Z_0\omega_0}{2i(\omega_0 - \omega) + \gamma}. \tag{5.2}$$

The approximated impedance $\tilde{Z}(\omega)$ corresponds to the response function of an oscillator with quality factor $Q = \omega_0/\gamma$, which confirms the role γ as the rate

of photon lost. It is sufficient to only take emission into account because most photon detectors work by detecting emitted photons. From the power dissipated over the detection part $P_\omega(t)$, we can determine an expression for the photon number rate $n(t)$ being emitted at time t into the transmission line. We can express the photon number rate in a frequency interval $[\omega, \omega + d\omega]$ by $dn(t) = P_\omega(t)d\omega/2\pi\hbar\omega$. The frequencies ω have to be positive, which corresponds to power dissipation into the transmission line. We should also mention that the expression depends on frequency and time, whereas we expect an expression to be either in frequency space or in the time domain. However, here we only ask the question of which frequencies a signal consists mainly at a given time. Therefore, we introduce

$$P_\omega(t) = \mathrm{Re}(Z_\omega^{-1}) \int d\delta \; V(t - \delta/2)V(t + \delta/2)e^{i\omega\delta}, \tag{5.3}$$

which captures a time and a frequency dependency of the signal. For this expression, we used that the dissipated power over a impedance Z is given by $P(t) = \mathrm{Re}(Z^{-1})V^2(t)$. Expressing the voltage $V(\omega) = Z(\omega)I(\omega)$ in the frequency domain, we receive the expression

$$n(t) = \iint \frac{d\omega d\nu}{2\pi e^2} \; \alpha_\omega Z^*(\omega + \nu/2)Z(\omega - \nu/2)I^-_{\omega+\nu/2}I^+_{\omega-\nu/2}e^{i\nu t}, \tag{5.4}$$

with $\alpha_\omega = G_Q/Z_0Q\omega$. For large quality factors Q this can also be approximated by $\tilde{\alpha}_\omega = G_Q/Z_0Q\omega_0$. Here, the plus/minus-current operators are defined as introduced in (4.45) so that the frequencies are only positive. For the sake of readability, from now on we start to give the frequency arguments of the currents as lower indexes. We model the quantum point contact, the source of radiation, within the Landauer Büttiker formalism as introduced in Section 3.1. The current operators are then given by (3.13) and (3.14). However, detector theory tells us that only Keldysh ordered expression are measurable. If we now want to give statements about the photon counting statistics in this setup, especially the second-order coherence, we need to calculate Keldysh ordered second order irreducible photon number cumulants. These can be expressed by Keldysh ordered current cumulants so that we can use the results obtained in Chapter 4.

5.2 Average Photon Rate

The first quantity of interest is simply the average photon rate transferred into the transmission line. It can be calculated using the results for the second-order cumulant obtained in Section 4.4. When calculating the average photon number, we deal with the expression

$$\begin{aligned}\langle n(t)\rangle = \int_0^\infty \frac{d\omega}{2\pi e^2} \int d\nu \; \alpha_\omega Z^*_{\omega+\nu/2}Z_{\omega-\nu/2} \\ \times S^{(2)}_{-+}(\omega + \nu/2, \omega - \nu/2)\delta(\nu)e^{i\nu t}.\end{aligned} \tag{5.5}$$

The delta distribution $\delta(\nu) = \delta(-\omega - \nu/2 + \omega - \nu/2)$ origins from Section 4.2 Rule 5. It renders the average photon number time independent. This fits with the fact that the bias voltage V_0 is constant and we are dealing with a steady state. Therefore, the average photon number rate is constant and given by

$$\langle n \rangle = \int_0^\infty \frac{d\omega}{2\pi e^2}\, \alpha_\omega |Z(\omega)|^2 S^{(2)}_{-+}(\omega). \tag{5.6}$$

Here, the phase of the impedance $Z(\omega)$ does not influence the result. However, this is different when we later consider photon photon correlations. We split $S^{(2)}_{-+}(\omega) = S_{\mathrm{ex}}(\omega) + S_{\mathrm{th}}(\omega)$ into an excess noise part

$$\begin{aligned} S_{\mathrm{ex}}(\omega) &= \int_{-\infty}^{\infty} d\varepsilon\; RT\big\{\Delta(\varepsilon)\Delta(\varepsilon-\omega)\big\} \\ &= \frac{RT\sinh(\frac{\hbar\omega_0}{2k_B\vartheta})}{2\sinh(\frac{\hbar\omega}{2k_B\vartheta})}\left(\frac{\omega_0-\omega}{\sinh\big[\frac{\hbar(\omega_0-\omega)}{2k_B\vartheta}\big]} - \frac{\omega_0+\omega}{\sinh\big[\frac{\hbar(\omega_0+\omega)}{2k_B\vartheta}\big]}\right) \end{aligned} \tag{5.7}$$

and a thermal part

$$\begin{aligned} S_{\mathrm{th}}(\omega) &= T\int d\varepsilon\; 2 f_R(\varepsilon) g_R(\varepsilon-\omega) \\ &= \frac{2T\omega}{(e^{\hbar\omega/k_B\vartheta}-1)}. \end{aligned} \tag{5.8}$$

The thermal contribution vanishes for zero temperatures (justifying the name) because the denominator diverges for $\vartheta = 0$. At low temperatures $\vartheta \ll \hbar\omega_0/k_B$ and large quality factors, it is sufficient to use $S_{\mathrm{ex}}(\omega)$ and replace $Z(\omega)$ and α_ω by $\tilde{Z}(\omega)$ and $\tilde{\alpha}_\omega$. The average photon number is then given by

$$\langle n \rangle = \int_0^\infty d\omega\; \frac{G_Q Z_0 \gamma S_{\mathrm{ex}}(\omega)}{4(\omega_0-\omega)^2+\gamma^2}. \tag{5.9}$$

5.3 Photon Photon Correlation

In this Section, we want to explore the correlations between the photon count at a reference time $t_0 = 0$ and the photon count at the delay time $t = \tau$. For this purpose, we consider the time integrated Fano factor and also time resolved correlations. Our central aim is to first calculate $n^{(2)}(\tau) = \langle\langle{:}n(\tau)n(0){:}\rangle\rangle_n$ from which we can then construct the Fano factor and $g^{(2)}(\tau)$. Then, the latter is given by

$$g^{(2)}(\tau) = \frac{n^{(2)}(\tau)}{\langle n\rangle^2} + 1, \tag{5.10}$$

while the Fano factor is connected with the second-order coherence as shown in (2.13). It is important to note that the irreducible expectation value $\langle\langle\cdot\rangle\rangle_n$ has to be taken in respect to the photon-number-rate operators $n(\tau)$. Thus, there can be contributing terms that are reducible in respect to current operators as long as these current operators belong to different $n(\tau)$ operators.

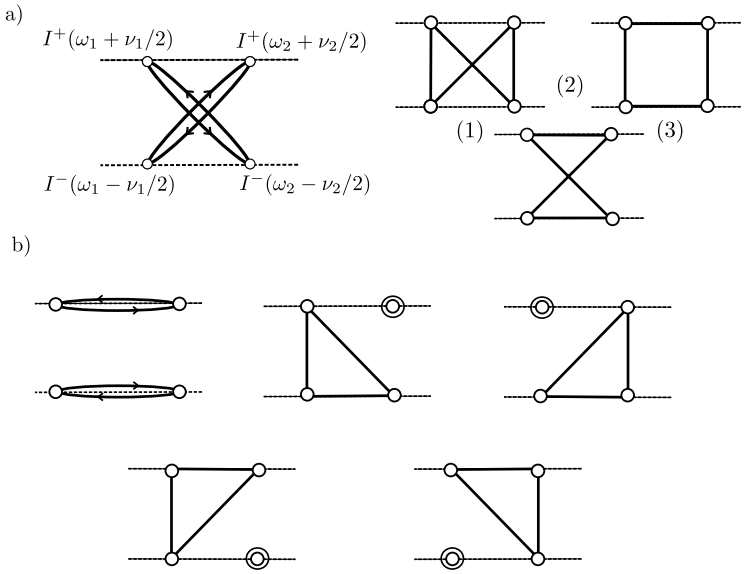

Figure 5.2: All possible photon number irreducible diagrams. The labeling of the currents is the same for all diagrams, shown only on the first one. The black circles around the empty white circles denote the contraction within the same current. In a) we show the contributing diagrams where the first one corresponds to the cumulant of the Gaussian $n_{\mathrm{G}}^{(2)}$ and the three diagrams on the right correspond to the cumulant of the non-Gaussian term $n_{\mathrm{nG}}^{(2)}$. The diagrams shown in b) are also photon number irreducible. However, all of them turn out to be zero, because they include loops solely contracted on one Keldysh contour, as explained in the main text. Thus, we only need to take the diagrams in a) into account.

Making use of the expression for the photon-number-rate operator in Eq. (5.4), we find

$$n^{(2)}(\tau) = \int \frac{d\omega_1 d\omega_2 d\nu_1 d\nu_2}{4\pi^2 e^4}\, \alpha_{\omega_1}\alpha_{\omega_2} Z^*_{\omega_1+\nu_1/2} Z_{\omega_1-\nu_1/2} Z^*_{\omega_2+\nu_2/2} Z_{\omega_2-\nu_2/2} \times \langle\langle I^-_{\omega_1+\nu_1/2} I^-_{\omega_2+\nu_2/2} I^+_{\omega_2-\nu_2/2} I^+_{\omega_1-\nu_1/2}\rangle\rangle_n e^{i\nu_1\tau}. \quad (5.11)$$

We can use the results that we already obtained for the current cumulants in Section 4.4. However, there we did not calculate n-irreducible but only current irreducible cumulants. A first step is to identify the contributing diagrams and express them via the results we already obtained. Fortunately, diagrams living only on one Keldysh contour branch are evaluated to be zero, as explained in Section 4.4. Thus, all diagrams containing an irreducible subdiagram with all current operators from only one contour branch do not need to be taken into account. This throws out all contributions with third-order current cumulants and one of the diagrams with second-order cumulants. In Figure 5.2, we show all diagrams which are n-irreducible and could in principle contribute, separated in the vanishing ones and the contributing ones. The contributing terms

can be decomposed into two parts, $n^{(2)}(\tau) = n_{\mathrm{G}}^{(2)}(\tau) + n_{\mathrm{nG}}^{(2)}(\tau)$, where the Gaussian term $n_{\mathrm{G}}^{(2)}(\tau)$ is a product of two second-order cumulants (first diagram in Figure 5.2 a)) and the non-Gaussian term $n_{\mathrm{nG}}^{(2)}(\tau)$ (three smaller diagrams in Figure 5.2 a)) consisting of three 4th-order current irreducible diagrams. The names origin from the fact that the Gaussian term is equivalent to an expression produced by Gaussian distributed currents. It is always positive and it is the dominating contribution at large temperatures so that it corresponds to the classical expectation. However, the non-Gaussian term can be also negative and can even dominate the Gaussian term for small temperatures. This makes photon antibunching possible because a negative $n^{(2)}(\tau)$ corresponds to a non-classical $g^2(\tau) < 1$. Above, we mentioned that the current through the QPC has to be spin polarized and the QPC has to be designed in a way so that only a single transverse channel may contribute. This can be explained with the competition of the Gaussian and the non-Gaussian term. Having more than one channel, we have to perform a sum over the different scattering channels for every closed loop (explained in Chapter 3). However, the classical Gaussian term consists of two closed loops, while the non-Gaussian term is current irreducible and consist of only one loop. Therefore, the Gaussian term scales with N_m^2, the total number of contributing modes m, whereas the non-Gaussian term scales only linearly with N_m. As the competition is head to head, already for a single mode, a second contributing mode is going to render the results classical.

We find the expressions for the Gaussian and the non-Gaussian term by inserting the corresponding diagrams into Eq. (5.11). Then, the Gaussian term reads

$$\begin{aligned} n_{\mathrm{G}}^{(2)}(\tau) &= \int_{\mathcal{G}} \frac{d\omega_1 d\omega_2 d\nu_1 d\nu_2}{4\pi^2 e^4}\, \alpha_{\omega_1}\alpha_{\omega_2} Z^*_{\omega_1+\nu_1/2} Z_{\omega_1-\nu_1/2} Z^*_{\omega_2+\nu_2/2} Z_{\omega_2-\nu_2/2} \\ &\qquad \times S_{-+}(\omega_1+\nu_1/2) S_{-+}(\omega_2+\nu_2/2) \delta(\omega_1-\omega_2)\delta(\nu_1+\nu_2) e^{i\nu_1\tau} \\ &= \int_{\mathcal{G}} \frac{d\omega_1 d\nu_1}{4\pi^2 e^4}\, \alpha^2_{\omega_1} \left|Z_{\omega_1-\nu_1/2}\right| \left|Z_{\omega_1+\nu_1/2}\right| \\ &\qquad \times S_{-+}(\omega_1+\nu_1/2) S_{-+}(\omega_1-\nu_1/2) e^{i\nu_1\tau}, \end{aligned} \tag{5.12}$$

where $\mathcal{G}$ is the region in which the frequency arguments of all Z-functions are positive. In the first line, we have replaced $\delta(\omega_2 - \omega_1 - \nu_1/2 - \nu_2/2)\delta(\omega_1 - \omega_2 - \nu_1/2 - \nu_2/2)$, which result from the diagram rules in Chapter 4, by the equivalent $\delta(\omega_1-\omega_2)\delta(\nu_1+\nu_2)$. Except from the complex exponential, 5.12 is a real term that is symmetric under the transformation $\nu_1 \mapsto -\nu_1$. After exploiting these properties and doing a variable substituiton in the frequencies, we can rewrite the Gaussian term as

$$n_{\mathrm{G}}^{(2)}(\tau) = \iint_0^\infty \frac{d\omega_1 d\omega_2}{4\pi^2 e^4}\, \alpha^2_{(\omega_1+\omega_2)/2} \left|Z_{\omega_2}\right| \left|Z_{\omega_1}\right| S(\omega_1) S(\omega_2) \cos(\omega_1-\omega_2). \tag{5.13}$$

With the given form of (5.13), we can immediately see that the result is real, as expected. Similar as for the plane photon number (5.6), the result does not

depend on the phases of the impedance. This is different for the non-Gaussian term $n^{(2)}_{\mathrm{nG}}(\tau)$, which reads

$$n^{(2)}_{\mathrm{nG}}(\tau) = \int \frac{d\nu}{4\pi^2} \iint_{|\nu|/2}^{\infty} d\omega_1 d\omega_2 \; Z(\omega_1, \omega_2, \nu) \\ \times (S_{1--++} + S_{2--++} + S_{3--++}) \cos(\nu\tau), \tag{5.14}$$

where we have suppressed the frequency argument of

$$S_{i--++} = S_{i--++}(\omega_1 + \nu/2, \omega_2 - \nu/2, \omega_2 + \nu/2, \omega_1 - \nu/2). \tag{5.15}$$

The phase dependence, which is given through the impedance, is provided by the function

$$Z(\omega_1, \omega_2, \nu) = \alpha_{\omega_1}\alpha_{\omega_2}\mathrm{Re}(Z^*_{\omega_1+\nu/2} Z_{\omega_1-\nu/2} Z^*_{\omega_2-\nu/2} Z_{\omega_2+\nu/2}). \tag{5.16}$$

The integration boundaries correspond to the region $\mathcal{G}$, where all the involved current frequencies are positive so that

$$\omega_1 + \nu/2 > 0, \;\; \omega_1 - \nu/2 > 0, \;\; \omega_2 + \nu/2 > 0, \;\; \omega_2 - \nu/2 > 0. \tag{5.17}$$

To find the form of the non-Gaussian term as given in 5.14, we have been using some symmetries, explained in the following. In 5.14, we have already performed one of the frequency integrals, which has been canceled by the Dirac delta distribution $\delta(\nu_1 + \nu_2)$ (which moreover is a result of Rule 5 in Chapter 4). This sets $\nu_2 \mapsto -\nu_1 = -\nu$. Additionally, it shows that also the non-Gaussian term is invariant under the transformation $\nu \mapsto -\nu$ because choosing $\nu_1 \mapsto -\nu_2 = -\nu$ from the delta distribution instead of the choice above, is equivalent to $\nu \mapsto -\nu$. Using this symmetry, we can show that the cumulant inside the non-Gaussian term is also invariant under the exchange of the two frequencies ω_1 and ω_2. We have

$$\begin{aligned} C^{(4)}_{--++} &= \langle\langle I^-_{\omega_1+\nu/2} I^-_{\omega_2-\nu/2} I^+_{\omega_2+\nu/2} I^+_{\omega_1-\nu/2} \rangle\rangle \\ &= \langle\langle I^-_{\omega_2-\nu/2} I^-_{\omega_1+\nu/2} I^+_{\omega_1-\nu/2} I^+_{\omega_2+\nu/2} \rangle\rangle \\ &= \langle\langle I^-_{\omega_2+\nu/2} I^-_{\omega_1-\nu/2} I^+_{\omega_1+\nu/2} I^+_{\omega_2-\nu/2} \rangle\rangle, \end{aligned} \tag{5.18}$$

where we commuted the two minus currents and the two plus currents among each other for the first equation mark. We are allowed to do so because the in-out ordering takes care about their correct ordering later on. Then, for the second equation mark, we used the symmetry under $\nu \mapsto -\nu$. With the two shown symmetries, it is straight forward to show that

$$\alpha_{\omega_1}\alpha_{\omega_2} Z^*_{\omega_1+\nu_1/2} Z_{\omega_1-\nu_1/2} Z^*_{\omega_2+\nu_2/2} Z_{\omega_2-\nu_2/2} \tag{5.19}$$

reduces to $Z(\omega_1, \omega_2, \nu)$ and $\exp(i\nu\tau)$ to $\cos(\nu\tau)$.

An important feature of the non-Gaussian term is that due to the phase dependence of $Z(\omega_1, \omega_2, \nu)$, the term can either be negative or positive. It has been shown that for low temperatures and an impedance peaked in the

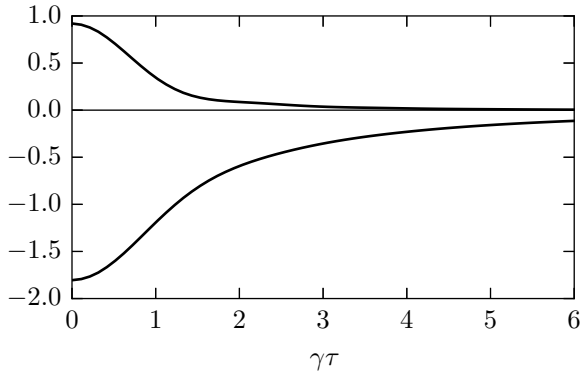

Figure 5.3: Plot of normalized Gaussian and non-Gaussian term. The upper curve corresponds to the classical $n_{\mathrm{G}}^{(2)}(\tau)/\langle n\rangle^2$ and the lower curve to $n_{\mathrm{nG}}^{(2)}(\tau)/\langle n\rangle^2$ at zero temperature. If the resulting second-order coherence is classical or non-classical relies on the competition of these two terms. Here, for zero temperature, we see that the negative non-Gaussian term dominates the positive Gaussian term.

frequency interval $[eV_0/2\hbar, eV_0/\hbar]$, its contribution is negative and can dominate the Gaussian term [19]. Therefore, we choose the resonance frequency $\omega_0 = eV_0/\hbar$. In this case $n^{(2)}(\tau)$ is negative for sufficiently small temperatures and therefore we find $g^{(2)}(\tau) < 1$, showing non-classical behavior.

Since we are interested in low temperature results, we approximate the full S_{i--++} by the low temperature and only out-current cumulants $\tilde{S}^{\mathrm{oooo}}_{i--++}$, as calculated in (4.49). Inserting the correct frequencies in the expression, we find

$$\tilde{S}^{oooo}_{1--++} = -2R^2T^2 \int d\varepsilon\ \Delta(\varepsilon - \tfrac{1}{2}\nu)\Delta(\varepsilon + \tfrac{1}{2}\nu)\Delta(\varepsilon + \omega_1)\Delta(\varepsilon + \omega_2),$$

$$\begin{aligned}
\tilde{S}^{oooo}_{2--++} =& -2R^2T^2 \int d\varepsilon\ \Delta(\varepsilon)\Delta(\varepsilon + \omega_1 + \tfrac{1}{2}\nu)\Delta(\varepsilon + \omega_2 + \tfrac{1}{2}\nu) \\
&\times \Delta(\varepsilon + \omega_1 + \omega_2), \\
\tilde{S}^{oooo}_{3--++} =& (RT - 2R^2T^2) \int d\varepsilon\ \Delta(\varepsilon)\Delta(\varepsilon + \omega_2 + \tfrac{1}{2}\nu)\Delta(\varepsilon + \omega_2 - \tfrac{1}{2}\nu) \\
&\times \Delta(\varepsilon + \omega_1 + \omega_2),
\end{aligned} \tag{5.20}$$

However, at $\vartheta = 0$, we can use the constraints on the frequencies to simplify the expressions even further. From the integration region of (5.14), we know $\omega_i \geq |\nu|/2$. With this and the fact that the $\Delta(\varepsilon)$ functions are step functions

(for zero temperature), we can rewrite

$$\tilde{S}^{oooo}_{1--++} = -2R^2T^2 \int d\varepsilon\ \Delta(\varepsilon + \tfrac{1}{2}|\nu|)\Delta(\varepsilon+\omega_1)\Delta(\varepsilon+\omega_2),$$

$$\begin{aligned}\tilde{S}^{oooo}_{2--++} &= -2R^2T^2 \int d\varepsilon\ \Delta(\varepsilon)\Delta(\varepsilon+\omega_1+\omega_2),\\ \tilde{S}^{oooo}_{3--++} &= (RT - 2R^2T^2)\int d\varepsilon\ \Delta(\varepsilon)\Delta(\varepsilon+\omega_1+\omega_2).\end{aligned} \tag{5.21}$$

For the case of $T = \frac{1}{2}$, which we use for all plots in this work, we find that $\tilde{S}^{oooo}_{2-,-,+,+} + \tilde{S}^{oooo}_{3-,-,+,+} = 0$ so that we are only left with the most important of the non-Gaussian terms. The ε integration can now easily be performed so that the non-Gaussian term is given by

$$n^{(2)}_{\mathrm{nG}}(\tau) = -\frac{2R^2T^2}{\pi^2}\int_{\mathcal{R}} d\nu d\omega_1 d\omega_2\ (\omega_0 - \tfrac{1}{2}\nu - \omega_2) Z(\omega_1,\omega_2,\nu)\cos(\tau\nu), \tag{5.22}$$

where $\mathcal{R}$ is the region $0 < \frac{1}{2}\nu < \omega_1 < \omega_2 < \omega_0 - \frac{1}{2}\nu$. Approximating also the Gaussian term with the corresponding zero temperature cumulants from (4.25) and performing the ε integration, we find

$$\begin{aligned}n^{(2)}_{\mathrm{G}}(\tau) =& \frac{R^2T^2}{4\pi^2}\iint_0^{\omega_0} d\omega_1 d\omega_2\ (\omega_0-\omega_1)(\omega_0-\omega_2)\\ &\times \alpha^2_{(\omega_1+\omega_2)/2}\,|Z_{\omega_1}|^2\,|Z_{\omega_2}|^2\cos[(\omega_1-\omega_2)\tau].\end{aligned} \tag{5.23}$$

In Figure 5.3, we show a plot of the Gaussian and non-Gaussian term at $\vartheta = 0$.

With the correct expressions at hand, we want to find a critical temperature, below which the non-Gaussian term dominates the Gaussian term and thus non-classical light should be involved in the physical processes. To clarify this question, we first make the connection to existing work [20] and calculate the Fano factor in the next section.

5.4 Critical Temperature from Fano Factor

In this section, we find a critical temperature ϑ_c below which the Fano factor is found smaller than one and thus giving rise to the occurrence of non-classical light. For a Fano factor smaller than one, the time integrated $N^{(2)} = \int d\tau\ n^{(2)}(\tau)$ has to be negative and so also the integrand has to be negative at some times τ. Thus, with a negative Fano factor, we know that at some time during the measurement the source was emmiting non-classical light. With $\int d\tau\ \cos(\tau\nu) = 2\pi\delta(\nu)$ the time integrated $N^{(2)}$ is quiet similar to the already calculated expression of $n^{(2)}(\tau)$ just without the cosine factor and one less frequency integral. The expressions $N^{(2)}_{\mathrm{G}}$ and $N^{(2)}_{\mathrm{nG}}$ correspond to the time integrated Gaussian and the non-Gaussian term (5.23) and (5.22). They are given at zero temperature by

$$N^{(2)}_{\mathrm{G}} = \frac{R^2T^2}{2\pi}\int_0^{\omega_0} d\omega\ (\omega_0-\omega)^2\alpha^2_\omega\,|Z_\omega|^4\,, \tag{5.24}$$

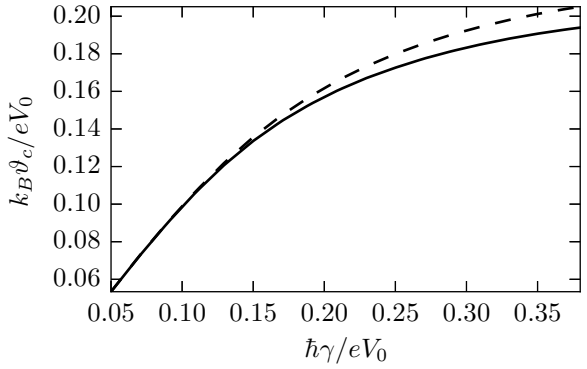

Figure 5.4: Critical temperature ϑ_c as a function of the inverse quality factor $Q = eV_0/\hbar\gamma$ obtained by numerical calculations. Below this temperature the Fano factor is lower than one. The dashed line corresponds to a result where we included all diagram terms for the calculation of the Fano factor. The solid line shows the critical temperature obtained by approximating the non-Gaussian term by (5.20). The difference between the 'exact' result and the approximation is very small, indicating the validity of the approximation. For large quality factors the curve is linear with $\vartheta_c \approx \hbar\gamma/k_B$.

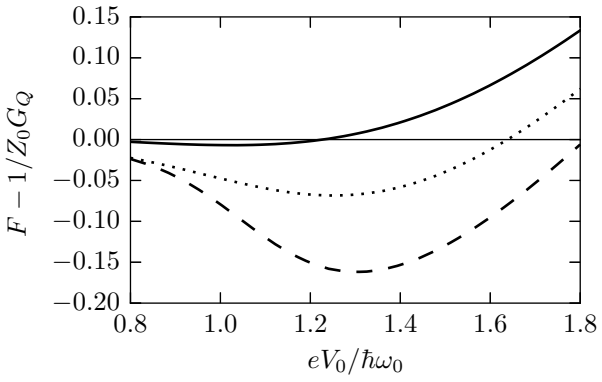

Figure 5.5: This plot shows the Fano factor plotted versus the bias voltage. The dashed line is plotted for $\vartheta = 0.05\hbar\omega_0$, the dotted line for $\vartheta = 0.10\hbar\omega_0$ and the solid line for $\vartheta = 0.15\hbar\omega_0$. Throughout this work, we set the bias voltage equivalent to the resonance frequency $eV_0 = \hbar\omega_0$ because this is the best choice for finding non-classical light in principle. However, for small enough temperatures, it can be useful to tune the bias voltage slightly out of resonance to strengthen the signal. Here, we see that the Fano factor becomes minimal for temperatures below $0.1\hbar\omega_0/k_B$ for about $eV_0 = 1.3\hbar\omega_0$. From this plot one can also see that it is correct to use a voltage in resonance to determine the critical temperature. In the vicinity of the critical temperature, the Fano factor, as a function of the voltage, is flat around ω_0 so that resonance is the correct choice.

and

$$N_{\mathrm{nG}}^{(2)} = -\frac{4R^2T^2}{\pi}\int_0^{\omega_0} d\omega_2 \int_{\omega_2}^{\omega_0} d\omega_1\ (\omega_0 - \omega_2) Z(\omega_1, \omega_2, 0). \tag{5.25}$$

Now we are interested in temperatures for which the non-Gaussian term dominates the Gaussian term so that $N^{(2)} = N_d^{(2)} + N_e^{(2)}$ is negative.

For this task we use numerics. With these, we can also reproduce the results obtained for the Fano factor in [20]. From the Fano factor data, we extract the critical temperature ϑ_c. In Figure 5.4, we show the latter depending on the inverse quality factor $Q = eV_0/\hbar\gamma$. There we compare two curves where one is obtained by a calculation involving all terms, while the second is obtained by using the approximated non-Gaussian term (5.20). The difference is very small, indicating that the approximation for the non-Gaussian term is valid in the shown regimes. For large quality factors the critical temperature is well approximated by $\vartheta_c \approx \hbar\gamma/k_B$. For smaller quality factors the curve starts to flatten out at about $\hbar\gamma/eV_0 = 0.2$. However, the results are not valid for too small quality factors because our model assumes the impedance of the transmission line to be constant over the range of γ. Therefore, $Q = 5$ seems to be a good compromise for real measurements, between having a high critical temperature and a still flat density of states in the transmission line.

The Fano Factor scales with the strength of the signal, as explained in Chapter 2. This makes it an indicator for the strength of the expected signal when doing an experiment. In this work, we do all calculations with the bias voltage set equal to the resonance frequency $eV_0 = \hbar\omega_0$, which is in principle the best choice for finding non-classical light. However, if we increase the bias voltage, we also strengthen the intensity and thus the number of photons arriving at the detector. This way, the Fano factor can be smaller for bias voltages slightly out of resonance, if the temperature is low enough ($\vartheta \lesssim 0.1\hbar\omega_0/k_B$). Therefore, we find the optimal bias voltage to make the Fano factor as small as possible (a large negative value) to be $V_0^* \approx 1.3\hbar\omega_0/e$. In Figure 5.5, we show a plot of the Fano factor depending on the bias voltage for different temperatures. In the next section, we show that with the time resolved second-order coherence function, we can give a less stringent constraint on the critical temperature.

5.5 Critical Temperature from Second-Order Coherence

The time averaged quantities like the Fano factor carry only a part of the physical information about the system. Therefore, in this section, we determine a critical temperature ϑ_c^* on the basis of the time resolved second-order coherence function $g^{(2)}(\tau)$. The critical temperature ϑ^* is defined as the temperature for which there is at least one point of time τ where $g^{(2)}(\tau) < 1$. Measuring around such times τ allows to find properties of non-classical light even if the Fano factor already approaches its classical value. In Figure 5.6 one can see numerically calculated $g^{(2)}(\tau)$ functions at different temperatures.

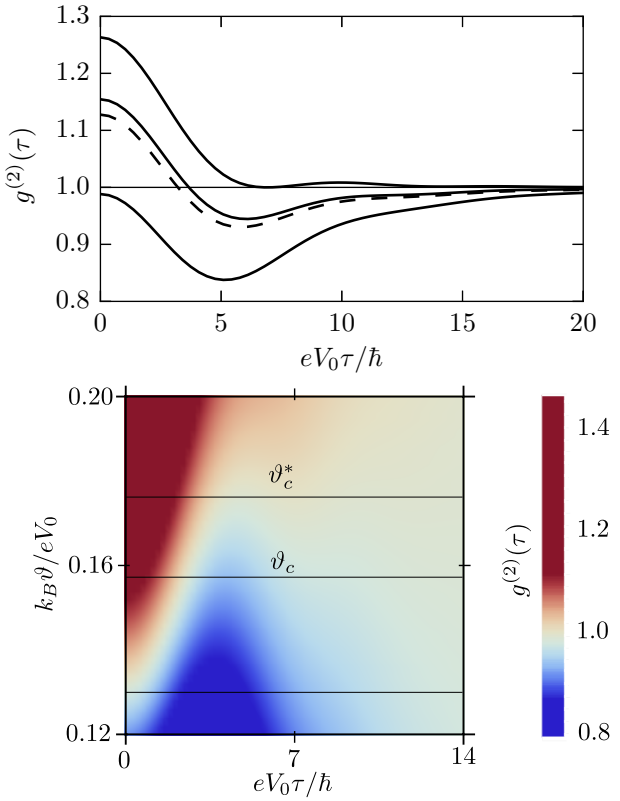

Figure 5.6: Upper Plot: The second-order coherence function $g^{(2)}(\tau)$ plotted for different temperatures with $\gamma = 0.2\hbar V_0$. The dashed curve is numerically calculated by including all diagram terms at the critical temperature $\vartheta_c = 0.157V_0/k_B$. The solid curves are calculated by only including the approximation (5.20) for the non-Gaussian term. They represent $g^{(2)}(\tau)$ from bottom to the top at $\vartheta = 0.130V_0/k_B$, $\vartheta_c = 0.157V_0/k_B$ and $\vartheta_c^* = 0.176V_0/k_B$. The comparison between the middle solid line and the dashed line shows that the approximation carries all important features and even underestimates the non-classical features by a few percent. The upper curve is calculated at exactly ϑ_c^* so that the minimum touches zero. For all curves above the two middle curves, we find the Fano factor $F > 1$. However, if measuring around the minimum for curves between the upper and the middle one, it is still possible to detect non-classical radiation. Lower Plot: This color plot represents $g^{(2)}(\tau)$ evaluated for different times and different temperatures. Blue colors denote a value below one while red colors denote a value above one. The horizontal lines correspond to the three temperatures in the upper plot. It can be seen that the minimum slightly persists up to ϑ_c^*. Above this temperature $g^{(2)}(\tau)$ starts to become monotone falling, approaching a value of one where all correlations are lost.

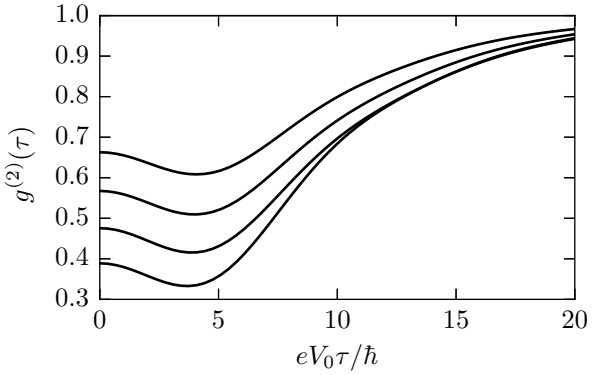

Figure 5.7: Second-order coherence $g(2)(\tau)$ at the temperature $\vartheta = 0.05e\omega_0/k_B$. The different curves are plotted for different values of $eV_0/\hbar\omega_0$. The upper curve corresponds to $eV_0/\hbar\omega_0 = 1.3$ going down in $eV_0/\hbar\omega_0 = 0.1$ steps for each line. The lowest line shows a plot in resonance $eV_0/\hbar\omega_0 = 1.0$, which validates that resonance is the best choice to observe the non classical properties of $g^{(2)}(\tau)$.

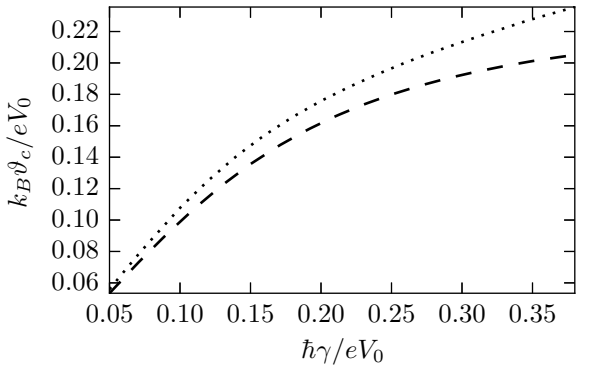

Figure 5.8: Critical temperature ϑ_c^* (dotted line) as a function of the inverse quality factor $Q = eV_0/\hbar\gamma$ compared to the critical temperature obtained for the Fano factor (dashed line). The critical temperature ϑ^* is defined as the temperature for which the second-order coherence is smaller than one for at least one single point of time. The plot shows that the constraint on the temperature from the Fano factor result can be relaxed for about 10%, if measured around the minimum of $g^{(2)}(\tau)$, as explained in the main text.

To evaluate the final results, we do numerical calculations here and implement the approximation (5.20). In our results $g^{(2)}(\tau)$ is monoton for $\vartheta = 0$ but if the temperature slightly rises, we always find a minimum around $\tau \approx 5\omega_0^{-1}$, which is caused by the dominance of the non-Gaussian term over the Gaussian term. The minimum can also be seen in Figure 5.6. We have numerically confirmed that this minimum and its behavior for changing temperatures is already captured in a simple law for $n^{(2)}(\tau)$, described in the following. The Gaussian term is almost unchanged by variations of the temperature. The non-Gaussian contribution however scales down if the temperature rises. Therefore, we can express

$$n^{(2)}(\tau) = n^{(2)}_{\mathrm{G}}(\tau, \vartheta = 0) + (1 - 0.6\frac{\vartheta}{\vartheta_c})n^{(2)}_{\mathrm{nG}}(\tau, \vartheta = 0), \tag{5.26}$$

which describes the temperature dependence of $n^{(2)}(\tau)$ in a very simple form.

Different from the Fano factor the value of $g^{(2)}(\tau)$ is normalized in respect to the squared signal intensity. Thus, we expect the non-classical features to become less pronounced if we choose a voltage V_0 out of resonance from ω_0. In Figure 5.7, we show $g^{(2)}(\tau)$ plotted for different values of V_0 while ω_0 is fixed (at $\vartheta = 0.05\omega_0\hbar/k_B$). As expected, we find the most non-classical result if the voltage is tuned in resonance with ω_0. However, when it comes to measurements, the signal strength is important and the Fano factor scaling with the signal should also be taken into account for the choice of the best measurement parameters, as explained in Section 5.4.

In Figure 5.8, we present the less stringent critical temperature ϑ_c^* extracted from our numerical results. The curve plotted against γ looks similar compared to the critical temperature plot from the Fano factor results alone. However, the plot suggests that it is possible to gain a win in the constraining temperature of about 10% compared to the data found by the Fano factor calculations. This means that measuring around the minimum of $g^{(2)}(\tau)$ can indeed help to find non-classical radiation in experiment.

Chapter 6

Conclusion

In this thesis, we have given a short introduction to the counting statistics of photons and within that have explained photon bunching and the HBT effect. For the latter, we have shown with an explicit example in Chapter 2 that it can already be understood classically. We have also demonstrated that common sources of radiation, like thermal radiation, follow super-Poissonian statistics which are also linked to the bunching of photons. Thus, it is interesting to consider photon antibunching, which is a quantum mechanical effect. Based on other work [19], we have suggested using a quantum point contact to produce antibunching radiation.

In Chapter 3, we have briefly discussed the Landauer Büttiker formalism for mesoscopic transport, which we have used to describe the transport properties of the QPC. In this context, we have introduced an energy independent scattering matrix, describing the transmission and reflection from the QPC, and have derived the polar decomposition in Appendix A. The latter allows to interpret the scattering matrix as the direct sum of the matrices for every scattering channel.

Furthermore, in Chapter 4, we have presented a novel diagrammatic approach to calculate current cumulants for energy independent scattering within the Landauer Büttiker formalism. We have given simple rules, derived in Appendix B, that can be used to calculate any orders of irreducible current cumulants in principle. Additionally, we have found methods to simplify the resulting expressions. With this we have provided the results for all current cumulants up to and including the third order and presented a 4th-order cumulant approximately. Especially the third-order cumulants are given more compact than found in literature [17].

Finally, we have presented a concrete theoretical model, based on [19], for a setup using a quantum point contact and an LC-filter for which the detection of non-classical radiation should be possible. By using our results for the current cumulants, we have calculated the Fano factor and estimated an optimal voltage regime with $V_0 \approx 1.3\hbar\omega_0/e$ to measure a maximal non-classical signal. Furthermore, we have determined a critical temperature below which the detection of non-classical radiation is possible. For a realistic quality factor $Q = 5$ this yield to be $\vartheta_c \approx 0.16\hbar\omega_0/k_B$. Then, we have calculated the second-

order coherence function as a time resolved quantity, which shows a minimum at $\tau \approx 5\omega_0^{-1}$. This minimum and the non-classical features in general, are an result of the competition of a Gaussian contribution and a non-Gaussian contribution. The latter scales down by a growing temperature while the former stays nearly unchanged, producing the mentioned minimum. Using this minimum as a criterion to find possible non-classical radiation, we have been able to define a less stringent expression for the critical temperature. It allows a raise in temperature of about 10% compared to the critical temperature obtained from the Fano factor.

As possible future work, the presented diagrammatic formalism could be generalized to non-energy independent transport. Additionally, it could possibly be used to resum the most important terms in a Dyson-like series to find the full counting statistics of photons emitted by a quantum point contact. In such a calculation, one could also include effects produced by switching-on and -off the bias voltage source.

Appendix A

The Scattering Matrix

In this work, the scattering matrix is an important object, as it provides the basis for the Landauer Büttiker formalism we use for all calculations. Therefore, we are going to highlight two aspects of it in this appendix. First, we want to derive the final energy independent form of the scattering matrix that we are using throughout this work. This can be done with the so called polar decomposition, for which one only rarely finds derivations in the literature. The second aspect, we want to talk about is the causality of the scattering matrix, which is important for the in-out current ordering formalism, replacing the Keldysh time-ordering.

As a starting point for the derivation of the polar decomposition, we use the singular value decomposition, which is a factorization possible for every matrix. It is well known and can be found in the literature. The statement is that an arbitrary matrix M can be written as

$$M = U^\dagger \Sigma V, \tag{A.1}$$

where $U^\dagger$ is a unitary matrix, Σ is a diagonal matrix with non-negative real numbers on its diagonal and V is also a unitary matrix. We start from the energy independent version of the scattering matrix

$$S = \begin{pmatrix} r & t' \\ t & r' \end{pmatrix} \tag{A.2}$$

and use the singular value decomposition on its four blocks so that we can write

$$\begin{aligned} r &= U_r^\dagger \sqrt{R} V_r, & r' &= U_{r'}^\dagger \sqrt{R'} V_{r'}, \\ t &= U_t^\dagger \sqrt{T} V_t, & t' &= U_{t'}^\dagger \sqrt{T'} V_{t'}. \end{aligned} \tag{A.3}$$

Here $\sqrt{R}$ and $\sqrt{T}$ are the non degenerate (which is physical), positive, diagonal matrices in a basis for which we order the entries by its size from the highest to the lowest. The notation is chosen with the square root to indicate that these matrices square to the matrices R and T. However, the singular value decomposition is not unique. We can define

$$\begin{aligned} U_\alpha'^\dagger &= U_\alpha^\dagger e^{i\Phi_\alpha} \\ V_\alpha' &= e^{-i\Phi_\alpha} V_\alpha, \end{aligned} \tag{A.4}$$

where $e^{i\Phi_\alpha}$ is a diagonal matrix with complex phases (complex entries with absolute value one) on its diagonal. Using the primed matrices corresponds to a change of basis because the phase matrices commute with the diagonal matrix and cancel each other. This gives rise to

$$U^\dagger \Sigma V = U'^\dagger \Sigma V'. \tag{A.5}$$

Now we return to our special case and analyze different matrix blocks of the scattering matrix products $S^\dagger S$ and $SS^\dagger$. Our aim is to find relations between the different U_α and V_α with $\alpha \in \{r, t, r', t'\}$, to then choose a simple basis. Thus, in the following, we first derive these relations. As S is unitary we can conclude

$$\begin{aligned} &(S^\dagger S)_{11} = r^\dagger r + t^\dagger t = 1 \\ \Leftrightarrow\ &V_r^\dagger R V_r + V_t^\dagger T V_t = 1, \\ \Leftrightarrow\ &R + V_r V_t^\dagger T V_t V_r^\dagger = 1, \end{aligned} \tag{A.6}$$

The matrix R and the right hand side are diagonal, therefore $V_r V_t^\dagger T V_t V_r^\dagger$ has to be also diagonal. Since T is already diagonal, we need to have $V_r = e^{i\Phi_1} V_t$ so that $V_t V_r^\dagger$ is also a unitary, diagonal matrix. From this we additionally find $R = 1 - T$. The second ordering results in

$$\begin{aligned} &(SS^\dagger)_{11} = r r^\dagger + t' t'^\dagger = 1 \\ \Leftrightarrow\ &U_r^\dagger R U_r + U_{t'}^\dagger T' U_{t'} = 1, \end{aligned} \tag{A.7}$$

from which we find in the same way as above $R = 1 - T'$ and $U_r = e^{-i\Phi_2} U_{t'}$. This also implies $T = T'$. Proceeding similar for the matrix block $(S^\dagger S)_{22}$, we find $R = R'$ and $V_{r'} = e^{i\Phi_3} V_{t'}$ and $U_{r'} = e^{-i\Phi_4} U_t$. We now have four degrees of freedom in choosing a convenient basis, which are given by the four diagonal phase matrices. However, the off-diagonal blocks of $SS^\dagger$ introduce one additional constraint. With

$$(SS^\dagger)_{12} = r^\dagger t' + t^\dagger r' = 0, \tag{A.8}$$

we have

$$\begin{aligned} &V_r^\dagger R U_r U_{t'}^\dagger T V_{t'} + V_t^\dagger T U_t U_{r'}^\dagger R V_{r'} = 0 \\ \Leftrightarrow\ &V_r^\dagger R e^{-i\Phi_2} T e^{-i\Phi_3} V_{r'} + V_r^\dagger e^{i\Phi_1} T e^{i\Phi_4} R V_{r'} = 0. \end{aligned} \tag{A.9}$$

Multiplying $V_r^\dagger$ from the left, $V_{r'}$ from the right, and then multiplying by $e^{i\Phi_3} e^{i\Phi_2}$, we find

$$RT[1 + e^{i(\Phi_1 + \Phi_2 + \Phi_3 + \Phi_4)}] = 0, \tag{A.10}$$

which turns out to be the only constraint on the phase matrices, because the second off-diagonal block only contains the same information. Now we can

choose a convenient basis, as long as we fulfill the constraint above. We choose $e^{i\Phi_3} = -1$ and $e^{i\Phi_1} = e^{i\Phi_2} = e^{i\Phi_4} = 1$ which fulfills (A.10). With this, we define

$$\begin{aligned} V &= V_r = V_t, \\ U &= U_r = U_{t'}, \\ U' &= U_{r'} = U_t, \\ V' &= V_{r'} = -V_{t'}. \end{aligned} \tag{A.11}$$

Now it is possible to write the scattering matrix in the singular value decomposition

$$S = \begin{pmatrix} U^\dagger \\ U'^\dagger \end{pmatrix} \begin{pmatrix} \sqrt{R} & \sqrt{T} \\ -\sqrt{T} & \sqrt{R} \end{pmatrix} \begin{pmatrix} V \\ V' \end{pmatrix}, \tag{A.12}$$

where the addition in the matrix product is meant as a direct sum. With this, we can use the unitary matrices U, U', V, V' to redefine the basis (and therefore the modes) of the scattering matrix like

$$\begin{aligned} \begin{pmatrix} \{b_l\} \\ \{b_r\} \end{pmatrix} &\mapsto \begin{pmatrix} U\{b_l\} \\ U'\{b_r\} \end{pmatrix}, \\ \begin{pmatrix} \{a_l\} \\ \{a_r\} \end{pmatrix} &\mapsto \begin{pmatrix} V\{a_l\} \\ V'\{a_r\} \end{pmatrix}, \end{aligned} \tag{A.13}$$

where $\{a_\alpha\}$ denotes the whole subspace of left- or right-labeled a-modes and similar for b-modes. As the transformation matrices are unitary, the commutation relations of the modes do not changes by this redefinition. Therefore, a basis of the scattering matrix can be chosen so that

$$S = \begin{pmatrix} \sqrt{R} & \sqrt{T} \\ -\sqrt{T} & \sqrt{R} \end{pmatrix}. \tag{A.14}$$

As the four subspaces in S are diagonal, we can rearrange them to separated blocks and write

$$S = \bigoplus_m \begin{pmatrix} \sqrt{R_m} & \sqrt{T_m} \\ -\sqrt{T_m} & \sqrt{R_m} \end{pmatrix}, \tag{A.15}$$

where R_m and T_m are real numbers between zero and one. They describe the reflection (R_m) and transmission (T_m) probability of the mth mode. The scattering matrix as given in (A.15) is the final form that we use throughout this work.

As already mentioned, the scattering matrix does not only connect the outgoing states with the incoming states but it also ensures causality. However, this can only be done by an energy dependent scattering matrix, which is physically always present. In our energy free approximation for the scattering matrix, we need to find a way to still implement this causality, which can be achieved by using the in-out time-ordering formalism explained in Section 4.1. Here, we want to show how the current commutator relations, we present there, are

linked to the causality of the scattering matrix. For this we follow mainly [17]. In the real time domain, the scattering matrix connects the outgoing with the incoming states by the relation

$$b_{\alpha m}(t) = \sum_{\beta,m} \int d\tau \; S_{\alpha\beta;mn}(t-\tau) a_{\beta n}(\tau). \tag{A.16}$$

The scattering matrix has to vanish for $\tau \geq t$, because otherwise an incoming current could cause an outgoing current in the past, which is of course non-physical. With this property, we are going to find the commutation relations for in- and out-currents. Starting with

$$\begin{aligned}
&[I_{\text{in}}(t_1), I_{\text{out}}(t_2)] \\
&= e^2 \sum_k \sum_{\substack{m,n,\\ j,\alpha,\beta}} \iint \frac{d\omega_1}{2\pi} \frac{d\omega_2}{2\pi} \iint d\varepsilon_1 d\varepsilon_2 \; e^{-i\omega_1 t_1} e^{-i\omega_2 t_2} \\
&\quad \times \left[a^\dagger_{r,k}(\varepsilon_1) a_{r,k}(\varepsilon_1+\omega_1), a^\dagger_{\alpha,m}(\varepsilon_2) S^\dagger_{r\alpha;mj}(\varepsilon_2) S_{r\beta;jn}(\varepsilon_2+\omega_2) a_{\beta,n}(\varepsilon_2+\omega_2) \right].
\end{aligned} \tag{A.17}$$

Using the correct commutation relations for the annihilation and creation operators given in (3.4), we end up with

$$\begin{aligned}
&[I_{\text{in}}(t_1), I_{\text{out}}(t_2)] \\
&= e^2 \sum_k \sum_{\substack{m,n,\\ j,\alpha,\beta}} \iint \frac{d\omega_1}{2\pi} \frac{d\omega_2}{2\pi} \int d\varepsilon_1 \; e^{-i\omega_1 t_1} e^{-i\omega_2 t_2} \\
&\quad \times \left[a^\dagger_{r,j}(\varepsilon_1) S^\dagger_{rr;kj}(\varepsilon_1+\omega_1) S_{r\beta;jn}(\varepsilon_1+\omega_2+\omega_1) a_{\beta,n}(\varepsilon_1+\omega_2+\omega_1) \right. \\
&\qquad \left. - a^\dagger_{\alpha,m}(\varepsilon_1-\omega_2) S^\dagger_{r\alpha;mj}(\varepsilon_1-\omega_2) S_{rr;jk}(\varepsilon_1) a_{r,k}(\varepsilon_1+\omega_1) \right] \\
&= e^2 \sum_{j,k} \iint \frac{d\omega_1}{2\pi} \frac{d\omega_2}{2\pi} \int d\varepsilon_1 \; e^{-i\omega_1 t_1} e^{-i\omega_2 t_2} \\
&\quad \times \left[a^\dagger_{r,j}(\varepsilon_1) S^\dagger_{rr;kj}(\varepsilon_1+\omega_1) b_{r,j}(\varepsilon_1+\omega_2+\omega_1) \right. \\
&\qquad \left. - b^\dagger_{r,j}(\varepsilon_1-\omega_2) S_{rr;jk}(\varepsilon_1) a_{r,k}(\varepsilon_1+\omega_1) \right].
\end{aligned} \tag{A.18}$$

If we proceed with all the integrals, the expression writes

$$\begin{aligned}
[I_{\text{in}}(t_1), I_{\text{out}}(t_2)] = 2\pi e^2 \sum_{j,k} \big[& a^\dagger_{r,j}(t_1) S^\dagger_{rr;kj}(t_2-t_1) b_{r,j}(t_2) \\
& - b^\dagger_{r,j}(t_1) S_{rr;jk}(t_2-t_1) a_{r,k}(t_2) \big],
\end{aligned} \tag{A.19}$$

where $S(t_i)$ is the Fourier transform of $S(\omega_i)$. The causality of the scattering matrix with the argument $t_2 - t_1$ thus renders the commutator $[I_{\text{in}}(t_1), I_{\text{out}}(t_2)] = 0$ for all $t_1 \geq t_2$. With the same procedure, we find

$$\begin{aligned}
[I_{\text{in}}(t_1), I_{\text{in}}(t_2)] &= 0, \\
[I_{\text{out}}(t_1), I_{\text{out}}(t_2)] &= 0.
\end{aligned} \tag{A.20}$$

With these commutators the Keldysh time-ordering can be replaced by the in-out ordering, as explained in Section 4.1. Using the latter not only helps to proceed with the time-ordering in frequency space but also implements the correct causality even for energy independent scattering matrices.

Appendix B

Deriving the Diagrammatic Rules

In Chapter 4, we presented diagrammatic rules for the calculation of irreducible current cumulants. In this Appendix, we derive these rules and show their validity. With our choice of the basis and the approximation of energy independent scattering, the current operators are given by

$$I_{\mathrm{In}}(\omega) = e \int d\varepsilon a^{\dagger}_{R,\varepsilon} a_{R,\varepsilon+\omega} \tag{B.1}$$

and

$$I_{\mathrm{out}}(\omega) = e \int d\varepsilon \Big[R a^{\dagger}_{R,\varepsilon} a_{R,\varepsilon+\omega} - R^{\frac{1}{2}} T^{\frac{1}{2}} (a^{\dagger}_{L,\varepsilon} a_{R,\varepsilon+\omega} + a^{\dagger}_{R,\varepsilon} a_{L,\varepsilon+\omega}) + T a^{\dagger}_{L,\varepsilon} a_{L,\varepsilon+\omega} \Big]. \tag{B.2}$$

We want to derive the diagrammatic rules presented in Section 4.2 for the calculation of expressions like

$$\langle\langle I^{\eta_1}_{\mathrm{in/out}}(\omega_1) I^{\eta_2}_{\mathrm{in/out}}(\omega_2) ... I^{\eta_n}_{\mathrm{in/out}}(\omega_n) \rangle\rangle. \tag{B.3}$$

In Section 4.2, we explain how we translate expressions like (B.3) into diagrams. To complete this, we provide the derivation of the rules on how to find the mathematical expressions corresponding to each diagram. Here, we repeat every rules once again, to then explain its origin properly. The first rule is given by

1. Every line in a diagram corresponds to either an f- or g- function as defined in Eq. (3.1) and Eq. (3.2). Whenever a line points in the direction against the Keldysh contour, it corresponds to the Fermi function $\langle c^{\dagger}_{\alpha,x} c_{\alpha,x} \rangle = f_{\alpha}(x)$. Lines pointing the other way around represent $\langle c_{\alpha,x} c^{\dagger}_{\alpha,x} \rangle = g_{\alpha}(x)$. The full diagram is then a product of the functions evaluated for every line.

A directed line between two currents depicts the Wick contraction with the creation operator of the starting current and the annihilation operator of the final

current so that it corresponds to either $\langle c^\dagger_{\alpha,x} c_{\alpha,x}\rangle = f_\alpha(x)$ or $\langle c_{\alpha,x} c^\dagger_{\alpha,x}\rangle = g_\alpha(x)$. If we find an f- or a g-function depends on the ordering of the operators. When performing the Wick contractions, we must keep the order of the contracted operator pair untouched. Thus, if the starting current in a cumulant like (B.3) is located left from the end current, we choose an f-function and if it is located right from the end current, we choose a g-function. The ordering of the current on the Keldysh contour in the diagrams exactly reflects the ordering in the cumulant expression from the right to the left. Therefore, we can directly apply rule 1.

2. For every line connecting two out-currents, sum over the resulting Fermi function's index α and multiply the corresponding term by either R for $\alpha = r$ or with T for $\alpha = l$. For a line going from an in-current to an out-current, $\alpha = r$ is fixed. Additionally, multiply by a factor of R. For a line that connects two in-currents or runs from an out-current to an in-current $\alpha = r$ is also fixed, but without an additional factor.

To understand this rule, it is useful to imagine the currents having an exit and an entrance, where the exit is given by the creation operator $c^\dagger_{\alpha,x}$ and the entrance by the annihilation operator $c_{\alpha,x}$. For example the in-current in Eq. (B.1) has an r-labeled exit and an r-labeled entrance. From the Kronecker delta $\delta_{\alpha,\beta}$ in terms like

$$\langle c^\dagger_{\alpha,x} c_{\beta,x'}\rangle = f_\alpha(x)\delta(x-x')\delta_{\alpha,\beta}, \tag{B.4}$$

we see that we can only have finite results if we connect equivalent labeled exits and entrances. In contrast to the simple in-current, the out-current (B.2) has four different entrances and exits. There are two right- and two left-labeled entrances, with each one right- and one left-labeled exit. Whenever we enter (contract with corresponding operator) through one of the entrances (annihilation operator), we need to multiply the term by the corresponding factor R,T or $\sqrt{RT}$ from the current operator and must leave through the corresponding exit (using the corresponding creation operator for the next contraction).

We first look at the simple case of contracting two in-currents. Here, we only have r-labeled exits and entrances and thus a contraction within these currents can only lead to $g_r(x)$ or $f_r(x)$. Having an in-current connected to an out-current must also result in functions $\propto g_r(x)$ or $\propto f_r(x)$, because the in-current has only r-labeled exits. However, we need to multiply the result with either R or $-\sqrt{RT}$, dependent on which entrance we choose. When we choose the R entrance the exit is also r-labeled. Choosing the $\sqrt{RT}$ entrance(right-labeled) renders the next exit left labeled. Whenever we enter a right-labeled $\sqrt{RT}$ entrance, we need to enter a left-labeled $\sqrt{RT}$ entrance later again (so that the corresponding function will be left-labeled) to switch back to the label where we started from. Otherwise, we cannot close the diagram loop without rendering it zero. Thus, the factor $-\sqrt{RT}$ always comes squared canceling the minus sign. This way, we can always assign the R factor to the right-labeled line and the T factor to the left-labeled line, no matter which of the two choices we make. If we have a line connecting two out-currents, it can be left-labeled

and right-labeled because we can go from a right exit to a left entrance and vice versa. Summing over all possible combinations (paths we can take, to travel through a full closed loop in the diagram), translates into rule 2.

3. Evaluate the frequency argument of an f- or g-function by $\varepsilon + \bar{\omega}_i$, where $\bar{\omega}_i = \sum_{C_{ir}} \eta_j \omega_j$ is the sum over all frequencies of currents $I(\omega_j)$ along the contour C_{ir}. The contour C_{ir} is defined by the directed diagram lines, starting from an initial current $I(\omega_i)$ and ending at a reference current $I(\omega_r)$. Choose a fixed reference current for a diagram (for example the last current on the Keldysh contour). The initial current is the current, from which the line corresponding to the evaluated f- or g-function starts. The contour C_{ir} includes the frequency of the current where the contour ends and excludes the frequency of the current where it starts. As indicated by η_j, each frequency in $\bar{\omega}_i$ comes with a plus or minus sign, which is determined by the type of current (minus or plus current).

Rule 2 was a result of the Kronecker delta in (B.4), whereas rule 3 is a product of the Dirac delta distribution $\delta(x - x')$ when contracting two operators $c^\dagger_\alpha(x)$ and $c_\alpha(x')$. From (B.1) and (B.2) can be seen that the frequency argument ω of a current always appears in the argument of the annihilation operator in the form $\varepsilon + \omega$. Doing all contractions for an expression like (B.3) generates the delta distributions

$$\delta(\varepsilon_1 - (\varepsilon_2 + \eta_2\omega_2))\delta(\varepsilon_2 - (\varepsilon_3 + \eta_3\omega_3))...\delta(\varepsilon_n - (\varepsilon_1 + \eta_1\omega_1)), \tag{B.5}$$

where we labeled the variables of an arbitrary reference current with 1 and for the next currents with increasing numbers following an arbitrary but fixed direction on the diagram. The last current has to be connected to the first current again, producing the last delta distribution $\delta(\varepsilon_n - (\varepsilon_1 + \alpha_1\omega_1))$. In principle, we have to perform an ε integration for each current. With the help of the delta distributions, we can always reduce them to only one single integral. We can proceed from the right to the left, starting with performing the ε_n integral. This sets $\varepsilon_n = (\varepsilon_1 + \eta_1\omega_1)$. Now performing the ε_{n-1} integral sets $\varepsilon_{n-1} = (\varepsilon_1 + \eta_1\omega_1 + \eta_n\omega_n)$. This can be repeated until only the ε_1 integral and one delta distribution $\delta(\sum_0^n \eta_i\omega_i)$ is left. This way, we have $\varepsilon_i = \varepsilon + \bar{\omega}_i$, where $\bar{\omega}_i = \sum_{C_{ir}} \eta_j\omega_j$ contains all frequencies of the currents on the contour C_{ir} that is defined to run from the current I_i to the reference current I_1 by following the diagram lines. This is equivalent to Rule 3. It also explains the origin of the delta distribution containing all frequencies and the single ε integration as given in Rule 5 and Rule 6:

5. The expression contains a Dirac delta distribution of all contributing frequencies $\delta(\sum \eta_i\omega_i)$. For minus currents the frequency in the sum is subtracted while for plus currents, the corresponding frequency is added, as indicated by η_i.

6. Evaluate the integral $\int d\varepsilon$ over the full expression.

The next rule explains the sign of each diagram and is directly linked to the fermionic sign which enters for every operator swap while performing the Wick contractions.

4. The sign of each diagram is given by $(-1)^{n_f+1}$, where n_f is the number of f-functions in the expression.

To understand this rule, we consider the simple expression

$$c_1^\dagger c_1 c_2^\dagger c_2 .... c_m^\dagger c_m, \tag{B.6}$$

representing the relevant part of an m-current cumulant (with fermionic operators). When performing the Wick contractions following a given diagram, we start by contracting the first creation operator $c_1^\dagger$ of the current I_1 with the annihilation operator c_n of the current I_n given by the diagram. This contraction does not introduce any sign because for all possible combinations, we have an even number of operators between the two contracted operators. Then, we continue with the creation operator $c_n^\dagger$ of the current I_n. Dependent on the diagram, dictating the next contraction to result in an f- or g- function, we contract with an operator to the right (f-function) or to the left (g-function) in (B.6). If we contract with an operator on the right, this will introduce a minus sign. This is because we already contracted the c_n operator to the right of the $c_n^\dagger$ operator, thus the number of operators between $c_n^\dagger$ and the targeting operator (the annihilation operator c we contract with) is odd. However, when we contract with an operator to the left, we still always have an even number of operators between $c_n^\dagger$ and the target operator. Therefore, every time we evaluate a diagram line to be an f-function, we need to multiply by a factor of (-1), except for the very first f-function. This is equivalent to Rule 4.

7. Perform a sum $\sum_m$ where m labels the different reflection and transmission probabilities R_m and T_m of different transverse modes.

The last rule trivially follows from the explanation about the block structure of the scattering matrix in 3.1.

The diagrammatic rules derived in this appendix simplify the calculation of general current cumulants in the Landauer Büttiker formalism. They are valid for energy independent scattering. For energy dependent scattering one could derive similar rules, less specialized than the presented ones.

Appendix C

Overview: Current Cumulant Results

In this Appendix, we present the results we obtained for the current cumulants in Chapter 4 again to grant a better overview. From the results, together with the relations between differently ordered cumulants, it is possible to construct all second and third-order cumulants.

Second-Order Results:

$$S^{(2)}_{-+}(\omega_1) = \int d\varepsilon \left\{ RT\big[\Delta(\varepsilon)\Delta(\varepsilon-\omega_1)\big] + 2T\big[f_r(\varepsilon)g_r(\varepsilon-\omega_1)\big] \right\}$$

$$S^{(2)}_{++}(\omega_1) = \int d\varepsilon \left\{ RT\big[\Delta(\varepsilon)\Delta(\varepsilon+\omega_1)\big] + Tf_r(\varepsilon)\big[g_r(\varepsilon+\omega_1) + g_r(\varepsilon-\omega_1)\big] + f_r(\varepsilon)\big[g_r(\varepsilon+\omega_1) - g_r(\varepsilon-\omega_1)\big] \right\}$$

$$S^{(2)}_{--}(\omega_1) = [S^{(2)}_{++}(\omega_1)]^*$$

$$S^{(2)}_{+-}(\omega_1) = S^{(2)}_{-+}(-\omega_1)$$

Third-Order Results:

$$
\begin{aligned}
S^{(3)}_{-++}(\omega_1,\omega_2) = \int d\varepsilon\, \big\{ & -2RT^2\Delta(\varepsilon)\Delta(\varepsilon-\omega_1)\Delta(\varepsilon-\omega_2) \\
& + RT\big[f_l(\varepsilon)g_r(\varepsilon-\omega_1) - f_r(\varepsilon)g_l(\varepsilon-\omega_1)\big]\big\} \\
S^{(3)}_{+++}(\omega_1,\omega_2) = \int d\varepsilon\, \big\{ & -2RT^2\Delta(\varepsilon)\Delta(\varepsilon+\omega_1)\Delta(\varepsilon-\omega_2) \\
& + RT f_l(\varepsilon)\big[f_r(\varepsilon+\omega_2)g_l(\varepsilon-\omega_1) - f_r(\varepsilon-\omega_2)g_l(\varepsilon+\omega_1)\big] \\
& + RT f_r(\varepsilon)\big[f_l(\varepsilon-\omega_2)g_r(\varepsilon+\omega_1) - f_l(\varepsilon+\omega_2)g_r(\varepsilon-\omega_1)\big] \\
& + RT\big[f_l(\varepsilon)g_r(\varepsilon+\omega_1) - f_r(\varepsilon)g_l(\varepsilon+\omega_1)\big]\big\}
\end{aligned}
$$

$$
\begin{aligned}
S^{(3)}_{--+}(\omega_1,\omega_2) &= [S^{(3)}_{-++}(\omega_2-\omega_1,-\omega_2)]^* \\
S^{(3)}_{---}(\omega_1,\omega_2) &= [S^{(3)}_{+++}(\omega_1+\omega_2,-\omega_2)]^*
\end{aligned}
$$

$$
\begin{aligned}
S_{++-}(\omega_1,\omega_2) &= S_{-++}(\omega_1-\omega_2,\omega_2) \\
S_{+-+}(\omega_1,\omega_2) &= S_{-++}(\omega_2,\omega_1)
\end{aligned}
$$

Acknowledgements

I want to dedicate this space to all the people who supported me during the last year while I was preparing this thesis.

My special thanks go to my supervisor Prof. Dr. Fabian Hassler, who guided me through an endless amount of new information and lots of challenges. He put a lot of effort and patience into teaching me the ideas that were relevant for the research project and also ideas that were just interesting or of future importance. Beside the topics presented in this thesis, we had countless discussions about other problems that did unfortunately not find their way in here.

I also want to thank Jascha Ulrich, Christoph Ohm and Manuel Rispler who always had an open ear for all my questions and helped me many times. Furthermore, I thank Helene Barton for making the most complicated problems a lot simpler. Besides, I thank everybody in the IQI in Aachen for creating such a nice working atmosphere.

I also thank Arlisa Müller for proofreading this thesis. I additionally thank her and especially Jim for being at my side all the time.

Last but not least, I want to thank my parents, who always supported me. They made it possible that I could always concentrate on my studies.

Bibliography

[1] G. Baym, Acta Phys. Pol., B **29**, 1839 (1998).

[2] R. Hanbury Brown, Nature **178**, 1046 (1956).

[3] E. Brannen and H. I. S. Ferguson, Nature **178**, 481 (1956).

[4] E. M. Purcell, Nature **178**, 1449 (1956).

[5] F. Diedrich and H. Walther, Phys. Rev. Lett. **58**, 203 (1987).

[6] C. W. J. Beenakker and H. van Houten, Solid State Phys. **44** (1991).

[7] D. V. Averin and E. V. Sukhorukov, Phys. Rev. Lett. **95**, 126803 (2005).

[8] H. van Houten and C. W. J. Beenakker, Phys. Today **49**, 22 (1996).

[9] C. Gerry and K. P.L., *Introductory Quantum Optics*, Cambridge University Press, 2004.

[10] R. Loudon, *The Quantum Theory of Light*, Oxford University Press, 1992.

[11] C. Emary *et al.*, Phys. Rev. B **85**, 165417 (2012).

[12] Y. M. Blanter and M. Büttiker, Phys. Rep. **336**, 1 (2000).

[13] J. Negele and O. H., *Quantum Many Particle Systems*, Advanced Books Classics, 1998.

[14] Y. V. Nazarov and M. Kindermann, EPJ B **35**, 413 (2003).

[15] V. Beaud, G. M. Graf, A. V. Lebedev, and G. B. Lesovik, J. Stat. Phys. **153**, 177 (2013).

[16] S. Bachmann, G. M. Graf, and G. B. Lesovik, J. Stat. Phys. **138**, 333 (2010).

[17] J. Salo, F. W. J. Hekking, and J. P. Pekola, Phys. Rev. B **74**, 125427 (2006).

[18] C. W. Beenakker and H. Schomerus, Phys. Rev. Lett. **86**, 700 (2001).

[19] C. W. Beenakker and H. Schomerus, Phys. Rev. Lett. **93**, 096801 (2004).

[20] I. C. Fulga, F. Hassler, and C. W. J. Beenakker, Phys. Rev. B **81**, 115331 (2010).